Next Materials 8 (2025) 100831

Contents lists available at ScienceDirect

Next Materials

journal homepage: www.sciencedirect.com/journal/next-materials

Research article

Topological characterization, computational, spectroscopic (FT-IR, 1H, 13C NMR) exploration, chemical reactivity analysis of 6-(3,3-dimethyl-oxiran-2-ylidene)-5,5-dimethyl-hex-3-en-2-one

R. Mohamed Hisam [a], P. Rajesh [a,*], E. Dhanalakshmi [a], Jeffrin JA Laura [a], M. Prabhaharan [b], G. Jayaraman [c]

[a] Department of Physics, School of Basic Science, Vels Institute of Science and Technology & Advanced Studies, Pallavaram, Chennai, Tamil Nadu 600117, India
[b] Department of Physics, Saveetha School of Engineering, Saveetha Institute of Medical and Technical Sciences (SIMATS), Chennai, Tamil Nadu 602 105, India
[c] Department of Mathematics, School of Basic Sciences, Vels Institute of Science, Technology & Advanced Studies, Pallavaram, Chennai, Tamilnadu 600 117, India

ARTICLE INFO

Keywords:
FT-IR
UV-Vis
NBO
Molecular Docking
And DMO-hexenone

ABSTRACT

The multifunctional organic molecule 6-(3, 3-dimethyl-oxiran-2-ylidene)-5, 5-dimethyl-hex-3-en-2-one has the capacity for a wide range of chemical reactivity and potential medical applications, also including antimicrobial activity, antitumor effects and reactivity in drug design. This study focuses on its synthesis, characterization and biological assessment in order to assess its medicinal potential. The compound was synthesized utilizing an improved reaction sequence and confirmed structurally by GC-MS, UV-Visible and FTIR spectroscopy. Density Functional Theory (DFT) methods with the Becke 3-parameter, Lee-Yang-parr (B3LYP) method, 6–311 + +G (d, p) basis set was used to investigate the electronic structure including HOMO-LUMO analysis, vibrational modes and molecular characteristics. Mulliken atomic charge analysis identifies the distribution of electron density among the atoms. NBO analysis revealing stabilized interactions, while Molecular Electrostatic Potential (MEP) mapping identified reactive regions. The Electron Localization Function (ELF) and Localized Orbital Locator (LOL) analyses reveals details on electron distribution. Reduced Density Gradient (RDG) analysis provided insights into bonding and non-bonding interactions. AutoDock simulations demonstrated the compound's potential as an anticancer inhibitor. This is the first integrated computational and experimental analysis of DMO-hexenone, showing its electronic structure, spectroscopic characteristics and anticancer potential.

1. Introduction

Cancer, a category of disorders defined by unregulated cell development, has emerged as a major national health concern. India now ranks third in cancer incidence, with a projected increase from 1.49 million in 2023–2.2 million in 2025. The condition emerges as the growth of malignant cells from human lung tissues, which eventually form tumors that might be cancerous (malignant) or noncancerous (benign) [1]. Oxirane based compounds are commonly known as epoxides, which are organic compounds containing three-membered cyclic ether structure with an oxygen compounds bonded to two adjacent carbon atoms. The ring strain in the oxirane structure results from 60° bond angles, which are substantially less than the optimum tetrahedral angle of 109.5 ° making the ring extremely reactive and susceptible to nucleophilic assault. It provides a highly reactive site, which influences molecular reactivity and stability, as well as the compound's electrical characteristics and possible uses in chemical synthesis and biological activity [2]. The chemical formula for the green synthesis of DMO-hexenone is C12H18O2, and it has the following structures: oxirane (epoxide), enone (α, β-unsaturated carbonyl molecule), and alkene substitution (C═C bond), and a methyl group. The compound is notable for its structural complexity. DMO-hexenone's α, β-unsaturated ketone structure has an electrophilic core that allows for Michael addition reaction with nucleophilic groups like biological molecules like thiols and amines [3]. The addition of methoxy group, particularly at the 5- position, increases the bioactivity of DMO-hexenone, since such substitution are frequently associated with improved therapeutic effectiveness and bio availability. Preliminary studies have suggested that hexenone derivatives like DMO-hexenone have significant anti-inflammatory and antioxidant activities, making them promising

* Corresponding author.
E-mail address: rajesh.ncc5coy@gmail.com (P. Rajesh).

https://doi.org/10.1016/j.nxmate.2025.100831
Received 20 January 2025; Received in revised form 30 May 2025; Accepted 9 June 2025
Available online 23 June 2025

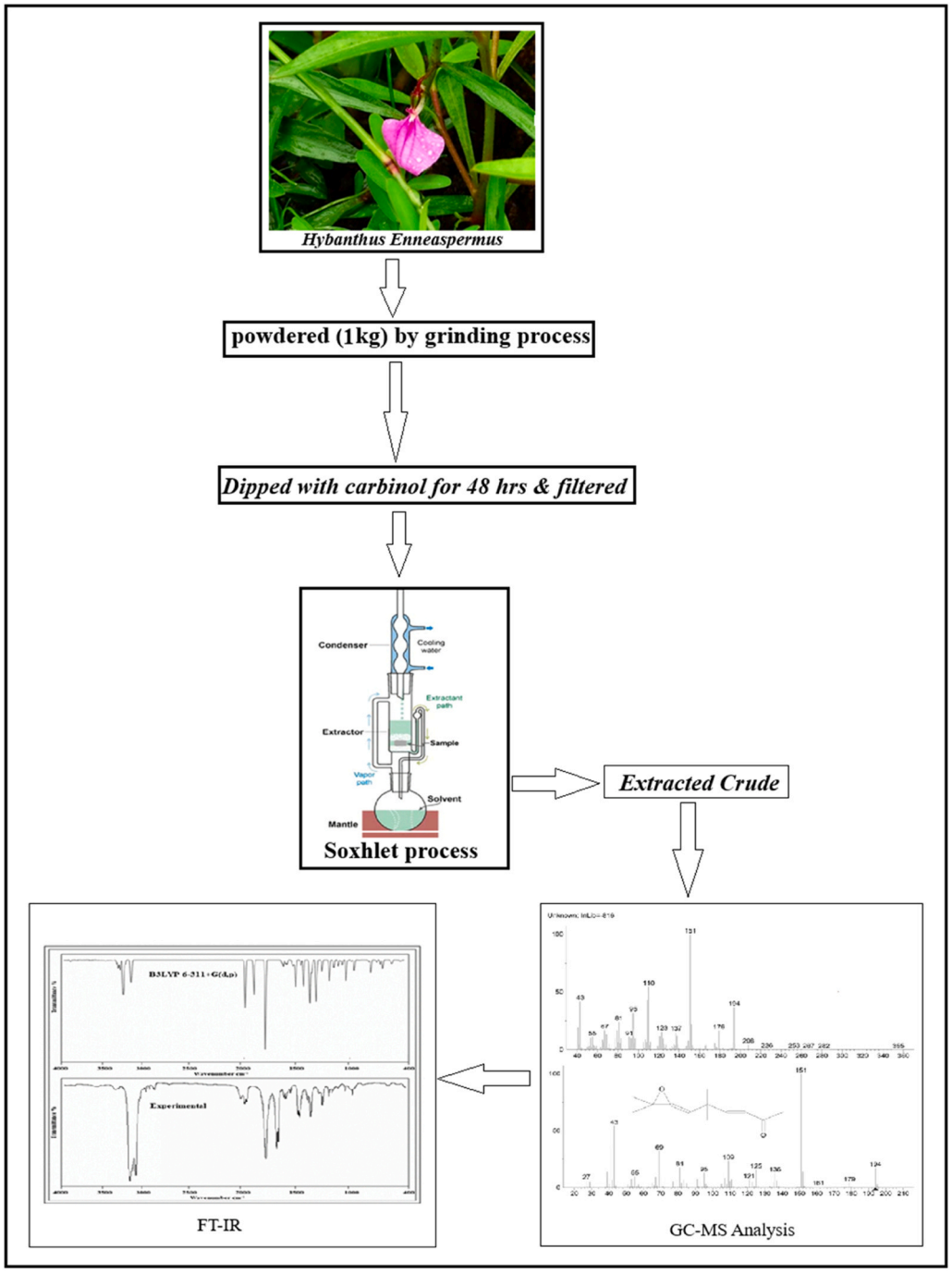

Scheme 1. Preparation of DMO-hexenone Compound from Carbinol Extract of Hybanthus Enneaspermus.

candidates for the treatment of diseases where inflammation and oxidative stress play key roles, such as cancer, cardiovascular conditions and neurodegenerative diseases [4]. According to evaluations of the literature, the *Hybanthus enneaspermus* plant may help with a number of ailments, such as inflammation, asthma, epilepsy, blood problems, coughing up blood, unpleasant diarrhoea, vomiting, burning sensations, daydreaming, urethral discharges, breast tone, and urinary infections [5]. *Hybanthus enneaspermus* is a plant that has traditionally been used in medicine but has yet to be recognized scientifically. We conduct this experiment to provide scientific evidence for its traditional use. Examining the *Hybanthus enneaspermus* ethanol leaf extract to find any possible adverse effects and bioactive ingredients. Rathanapurush in Sanskrit, Pursharathna in Hindi, and Orithazhthamarai in Tamil are its names [6]. The family Violaceae comprises the perennial herb *Hybanthus enneaspermus (L) F. Muell.* Ayurveda and Siddha, along with traditional treatments use *Hybanthus enneaspermus* aphrodisiac and anti-infertility characteristics to heal ailments [7]. Antiarthritic activity, CNS action, antiulcer, and antisecretory. It has been employed in several research avenues, including in vitro, in vivo, and clinical trials for hypolipidemic and antibacterial properties [8,9]. No reports of theoretical (DFT), spectroscopic, or molecular docking studies of recently synthesized materials came up in a review of the literature. We obtained a plant extract from *Hybanthus enneaspermus* and assessed its potential for cancer-related activities to conduct this investigation. The structural conformation and stability of molecules were examined using the GC-MS method. To describe the newly synthesized chemical, FT-IR

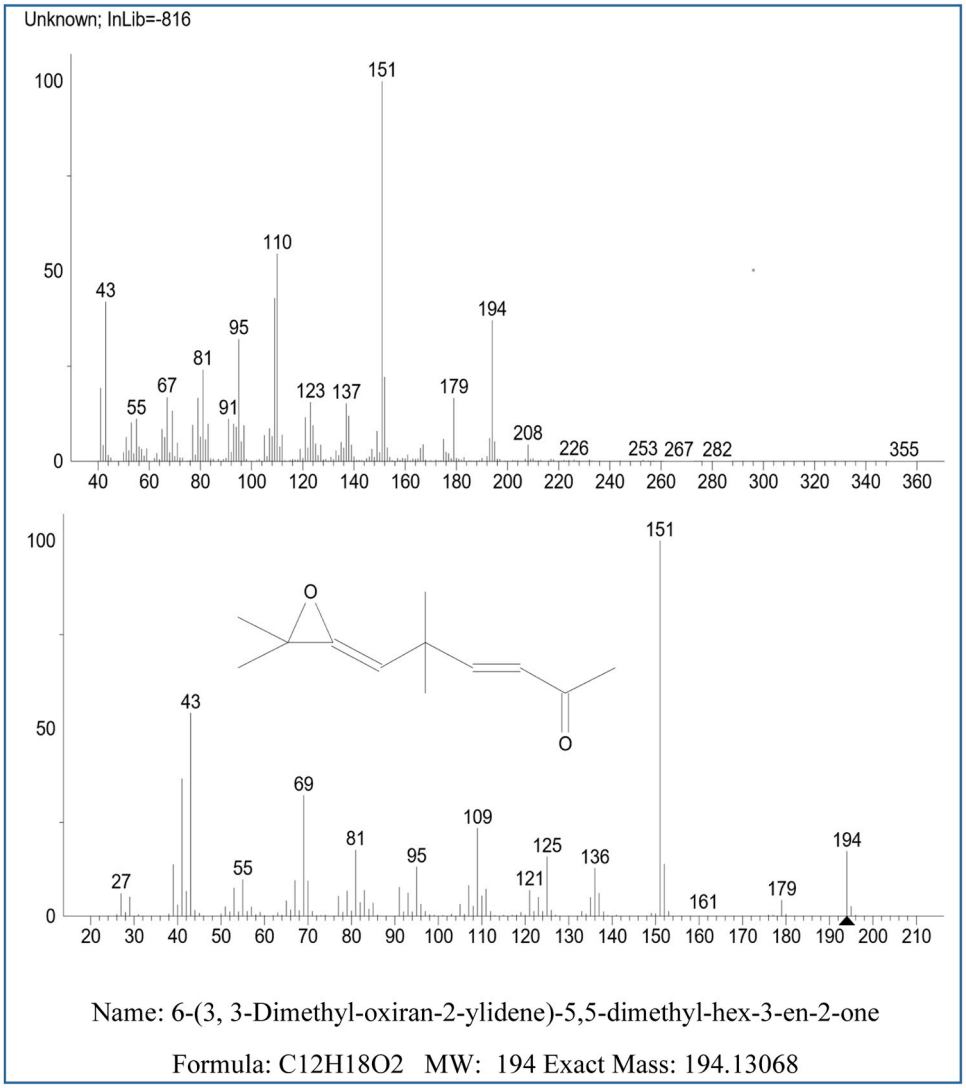

Fig. 1. GC–MS result of DMO-hexenone.

and UV–visible spectroscopy and 1H, and 13C NMR spectral techniques were used [10]. The optimized structural geometry and harmonic frequencies of the DMO-hexenone component were investigated using DFT/B3LYP simulations using the 6–311 + +G (d, p) basis set. An analysis of the DMO-hexenone molecules' HOMO-LUMO energy gap is carried out. NBO 3.1 tool was used to analyze the title compound's intermolecular interactions, hydrogen bonds, and charge delocalization. The electronic transition is computed using TD-DFT and compared to the measured UV–visible absorption spectra of the title chemical. One of the biggest challenge in medication for cancer is understanding the interactions between medicines and receptors. The mechanism of the drug-receptor complex was investigated utilizing molecular docking and in vitro cytotoxicity experiments [11]. The newly developed compound was docked against the MET4 and TRP47 receptors to assess its carcinogenic potential.

2. Green synthesis of the hybanthus enneaspermus plant

The Hybanthus enneaspermus plant was obtained in 3 kg from thalaiyari thangal village in Tiruvallur, Tamil Nadu, India. After three weeks of drying at room temperature, 1 kg of the dried plants were crushed using an electric grinder. The powder was dipped in carbinol 95.5 % at a 2:1 ratio and stored at room temperature for 48 h with occasional shaking after which the soxhlet process was used to separate crude, as stated in Scheme1.

3. Experimental techniques

The bioactive compound extraction from Hybanthus enneaspermus. The village of Thalaiyari Thangal in Tamil Nadu, India's Tiruvallur district, provided three kilograms of the medicinal herb Hybanthus Enneaspermus. The three kilograms of plants were allowed to dry at ambient temperature for three weeks before being processed using an electric grinder into a one-kilogram powder. The powder was shook repeatedly during the extraction process using 95.5 % carbinol for 72 h at room temperature. The crude and carbinol were separated using the Soxhlet method. The carbinol crude from Hybanthus enneaspermus was assessed by SRM University in Kattankulathur, Chengalpattu district, Tamil Nadu, India, using GC-MS (QP2010 Plus-Shimadzu). Numerous peaks on the GC-MS analysis graph indicate the discovery of multiple distinct chemicals. Sigma Aldrich provided the 99 % pure chemical DMO-hexenone, which we used as the only extraction component for our investigation. A Perkin Elmer FT-IR spectrophotometer was used to record the DMO-hexenone compound's FT-IR spectra in the 4000–400 cm^{-1} region using the KBr pellet technique. Using a Perkin Elmer Lambda 950 UV-Visible spectrophotometer, the absorption spectra of the MIP compound were also measured in the 200–300 nm region.

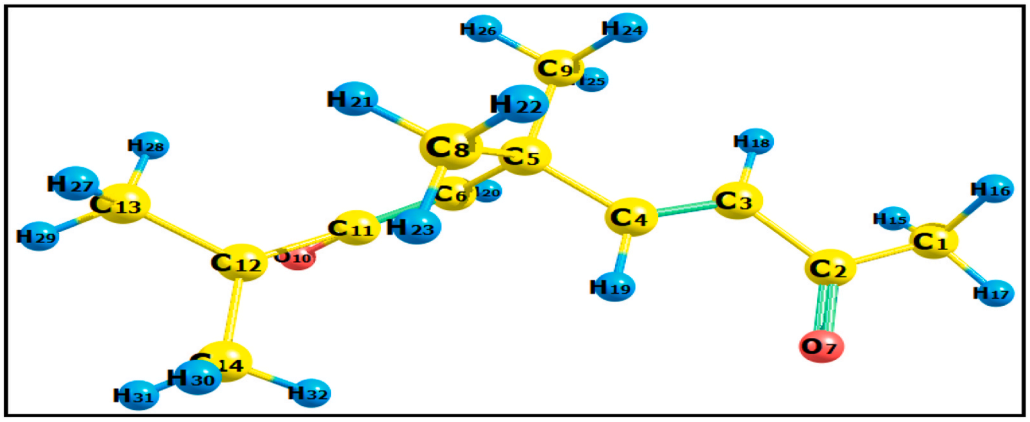

Fig. 2. Optimized Structure of DMO-hexenone.

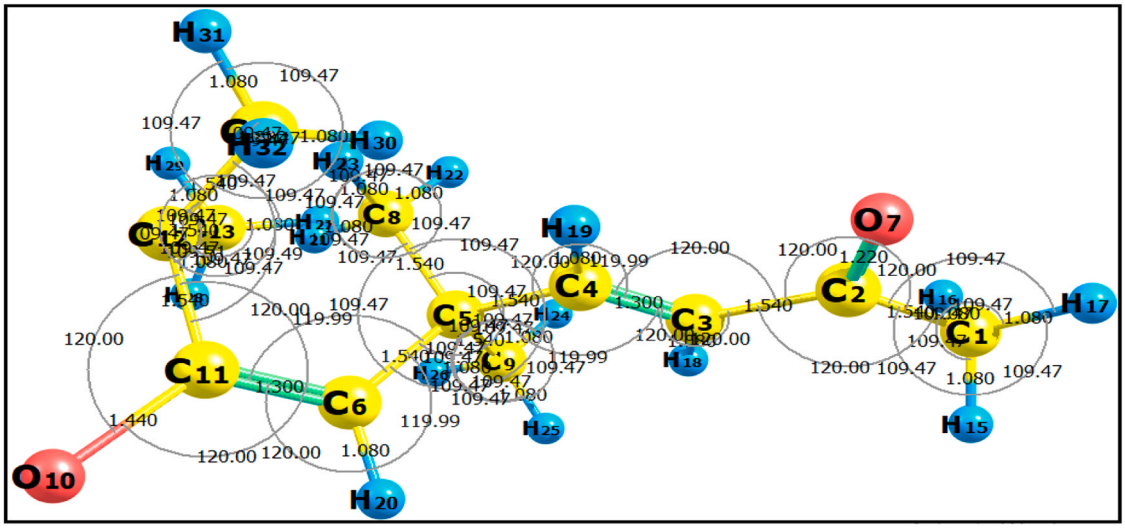

Fig. 3. Bond angle with optimized structure of DMO-hexenone.

4. Computational details

This paper used the Gaussian 09 W computer package to calculate the molecular sFtructure for 6DOYHO. The hybrid functional Becke-Lee, Parr, and Yang DFT/B3LYP technique is used to interpret the geometry parameters of bond length and bond angle at the 6–311 + +G (d, p) level [12,13]. GaussView 5.0 was used to view the vibrational wave numbers of the FT-IR spectra and their associated PED%. To ensure accuracy vibrational modes were checked via PED analysis, which confirmed the agreement between computed frequencies and experimental data. Veda 04 software was used for analysis. Additionally, molecular electrostatic potential (MEP) and HOMO-LUMO (Highest unoccupied Molecular Orbital-Lowest Unoccupied Molecular Orbital) plots were generated through these computational tools. [14]. The UV-Visible absorption spectra were simulated using time-dependent DFT (TD-DFT) at the hybrid B3LYP/6–311 + +G (d, p) level of theory. The B3LYP/6–311 + +G (d, p) basis set were chosen for, providing an appropriate balance between experimental and computational precision compared to any other basis sets [15]. The Natural Bond Orbital study is explained by second-order perturbation theory and includes charge transfer between donors and acceptors, intramolecular hydrogen bonding interactions, and hyperconjugate interactions [16]. In addition to Mulliken population analysis and the computation of NMR electronic properties, energy gap, electrophilicity index, and nucleophilicity index, the MEP surface was used to detect reactive sites [17]. Molecular docking investigation were carried out using AutoDock 1.5.6 software which assessed the binding energies of the ligand and protein complexes. In these docking simulations, a grid box was created around the protein's active site, with dimension sufficient to accommodate the ligand. The binding pocket was discovered using previously published research on protein-ligand interactions. To confirm the docking results, re-docking was done, and the root-mean square deviation and docked position was determined. Control ligands with known binding characteristics were employed as references to check the docking accuracy [18].

5. GC-MS analysis

Gas chromatography-mass spectrometry is a potent method for analyzing and effectively separating multicomponent mixtures with low concentrations. The GC-MS offers a wide range of applications, including pollution investigations, forensics, and purified bio molecules (fatty acids and lipids). The analysis was performed using Gas Chromatography-Mass Spectrometry (GC-MS) of the carbinol crude of *Hybanthus nneaspermus* identifies five primary peaks by comparing retention duration, concentration, peak area (%), peak height (%), and mass spectral fragmentation patterns with those of recognized compounds in the NIST database, bioactive compounds were found [19]. Title compound *(6-(3, 3-dimethyl-oxiran-2-ylidene)-5, 5-dimethyl-hex-3--en-2-one)* Fig. 1. GC-MS was used to identify it in the carbinol extract of

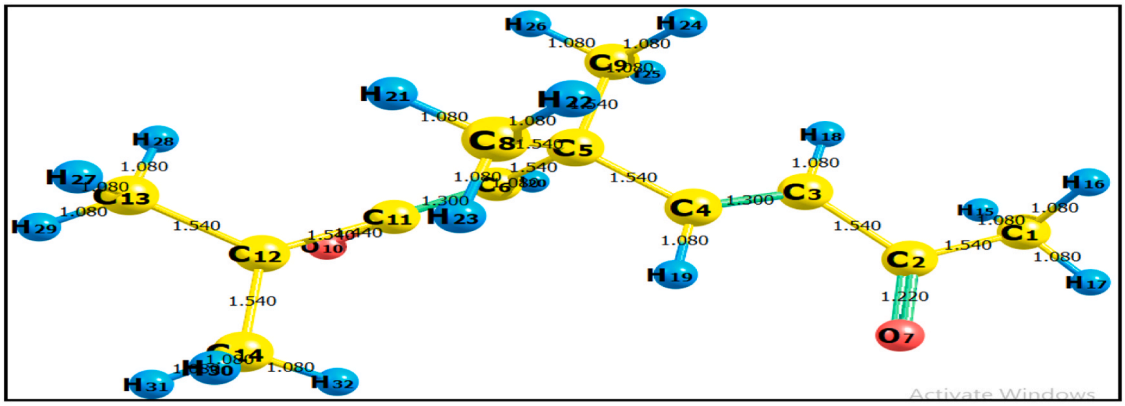

Fig. 4. Bond length with optimized structure of DMO-hexenone.

Table 1
Geometrical Parameter of DMO-hexenone.

Bond length (Å)	B3LYP/6–311 + +G(d,p)	Experimental	Bond Angle (o)	B3LYP/6–311 + +G (d, p)	Experimental
C_1-C_2	1.51	1.54	C_4-C_3-C_{18}	121.76	121.7
C_1-H_{15}	1.09	1.00	C_3-C_4-C_5	128.32	-
C_1-H_{16}	1.09	0.93	C_3-C_4-C_{19}	116.48	-
C_1-H_{17}	1.09	1.00	C_5-C_4-H_{19}	115.18	116
C_2-C_3	1.48	1.47	C_4-C_5-C_6	106.12	-
C_2-O_7	1.22	1.30	C_4-C_5-C_8	107.9295	-
C_3-C_4	1.34	1.30	C_4-C_5-C_9	112.6371	-
C_3-C_{18}	1.08	-	C_6-C_5-C_8	111.8438	-
C_4-C_5	1.51	1.5–1	C_6-C_5-C_9	108.9078	-
C_4-C_{19}	1.09	-	C_8-C_5-C_9	109.402	-
C_5-C_6	1.52	1.40	C_5-C_6-C_{11}	126.3088	123.7
C_5-C_8	1.54	1.50	C_5-C_6-H_{20}	116.439	-
C_5-C_9	1.54	1.50	C_{11}-C_6-H_{20}	117.2331	117.8
C_6-C_{11}	1.32	1.30	C_5-C_8-H_{21}	110.5165	108.9
C_6-H_{20}	1.08	0.90	C_5-C_8-H_{22}	110.3031	109.5
C_8-H_{21}	1.09	0.90	C_5-C_8-H_{23}	111.5084	116
C_8-H_{22}	1.09	1.00	H_{21}-C_8-H_{22}	108.2821	109.5
C_8-H_{23}	1.09	1.10	H_{21}-C_8-H_{23}	108.3354	109.5
C_9-H_{24}	1.09	-	H_{22}-C_8-H_{23}	107.787	107.7
C_9-H_{25}	1.09	-	C_5-C_9-H_{24}	111.1508	-
C_9-C_{26}	1.09	-	C_5-C_9-H_{25}	111.4623	-
O_{10}-C_{11}	1.36	1.39	C_5-C_9-H_{26}	110.0232	109.5
O_{10}-C_{12}	1.49	1.49	H_{24}-C_9-H_{25}	108.1721	-
C_{11}-C_{12}	1.44	1.45	H_{24}-C_9-H_{26}	108.2779	109
C_{12}-C_{13}	1.51	1.50	H_{25}-C_9-H_{26}	107.6272	-
C_{12}-C_{14}	1.51	1.48	C_6-C_{11}-O_{10}	137.0823	-
C_{13}-H_{27}	1.09	-	C_6-C_{11}-C_{12}	158.4812	-
C_{13}-H_{28}	1.09	1.00	O_{10}-C_{12}-C_{13}	113.741	-
C_{13}-H_{29}	1.09	0.99	O_{10}-C_{12}-C_{14}	113.7142	-
C_{14}-H_{30}	1.09	0.90	C_{11}-C_{12}-C_{13}	120.5426	121
C_{14}-H_{31}	1.09	-	C_{11}-C_{12}-C_{14}	120.3097	119
C_{14}-H_{32}	1.09	-	C_{13}-C_{12}-C_{14}	116.6912	118
Bond Angle (o)	**B3LYP/6 311 + +G(d,p)**	**Experimental**	C_{12}-C_{13}-H_{27}	110.2275	-
C_2-C_1-H_{15}	110.37	108.5	C_{12}-C_{13}-H_{28}	110.8917	-
C_2-C_1-H_{16}	110.38	109.5	C_{12}-C_{13}-C_{29}	110.3087	-
C_2-C_1-H_{17}	109.85	109.5	H_{27}-C_{13}-H_{28}	108.6699	-
H_{15}-C_1-H_{16}	106.83	107.9	H_{27}-C_{13}-H_{29}	107.8677	107.7
H_{15}-C_1-H_{17}	109.66	109.5	H_{28}-C_{13}-H_{29}	108.7992	109.5
H_{16}-C_1-H_{17}	109.67	109.4	C_{12}-C_{14}-H_{30}	110.2755	-
C_1-C_2-C_3	116.18	118.0	C_{12}-C_{14}-H_{31}	110.3095	109.5
C_1-C_2-O_7	121.36	120.0	C_{12}-C_{14}-H_{32}	110.9071	-
C_3-C_2-O_7	122.44	121.0	H_{30}-C_{14}-H_{31}	107.8146	107.8
C_2-C_3-C_4	120.84	120.8	H_{30}-C_{14}-H_{32}	108.6211	108.9
C_2-C_3-H_{18}	117.39	120.0	H_{31}-C_{14}-H_{32}	108.8343	107.7

Hybanthus enneaspermus research showed that the carbinol crude of the plant contains several bioactive components. The title compound is considered based on its uniqueness in anti-cancer activity and literature review. The NIST library discovered and identified the chemical compound DMO-hexenone [20]. GC-MS analysis confirmed the structure of the title molecule, which has a chemical formula of $C_{12}H_{18}O_2$, retention time of 44.022 min, and molecular weight of 194.13 g/mol.

Table 2
Mulliken atomic charges of DMO-hexenone.

Atom	Charges (a.u)	Atom	Charges (a.u)
C_1	−0.39384	H_{17}	0.133626
C_2	0.408306	H_{18}	0.078575
C_3	−0.14763	H_{19}	0.117332
C_4	−0.00318	H_{20}	0.097646
C_5	−0.02695	H_{21}	0.105693
C_6	−0.21946	H_{22}	0.109934
O_7	−0.46513	H_{23}	0.106263
C_8	−0.31812	H_{24}	0.102299
C_9	−0.30928	H_{25}	0.104907
O_{10}	−0.48751	H_{26}	0.10705
C_{11}	0.383024	H_{27}	0.117765
C_{12}	0.17741	H_{28}	0.128239
C_{13}	−0.32511	H_{29}	0.12085
C_{14}	−0.32712	H_{30}	0.117951
H_{15}	0.126426	H_{31}	0.120806
H_{16}	0.12531	H_{32}	0.133918

6. Result & discussion

6.1. Molecular geometry

The molecule's improved molecular shape is displayed in Fig. 2 coupled with the chemical structure and DMO-hexenone numbering. Using the 6–311 + +G(d, p) basis set and the Gaussian 09 programmed by the DFT/B3LYP method, geometrical parameters such as bond length and bond angle are determined. Figs. 3 and 4 displays the structurally optimized parameters corresponding to the experimentally observed XRD data [21]. The two co groups in the optimized molecular geometry used in this work—C2-O7, C1-C2-O7, C3-C2-O7, C6-C11-O10, O10-C12-C13, and O10-C12-C14—define the presence of carbonyl groups in the linear structures that contain carbons. The combination of the CC, CH, and CO of bond angle and bond length obtained in this title molecule also describes the correlation of the CCC, HCH, CCO, and CCH with maximum and minimum values that match the experimental XRD values [22]. The CC bond found has a maximum value of C5-C8, a minimum value of C6-C11, and an experimental value of 1.30 Å for C6-C9, and 1.54 Å for C5-C9. In the CH bond, C1-H15, C1-H16, C1-H17, C8-H21, C8-H22, C8-H23, C9-H24, C9-H25, C13-H27, C13-H28, C13-H29, C14-H31, C14-H32 has 1.09 Å with experimental values 1 Å, 0.93 Å, 0.90 Å similar to the obtained values shown in Table 1 and its minimum value of CH bond is C6-H20 contain 1.08 Å related to the experimental values 0.90 Å which is well matched [23]. In C2-O7, O10-C11, O10-C12 has 1.22 Å, 1.36 Å, 1.49 Å which is corresponding to the experimental values are 1.30 Å, 1.39 Å, 1.49 Å. For this title compound the bond angle were observer in various combination of carbon, hydrogen, oxygen atoms which is exhibit angle are listed below. In the CCC bond it attains the maximum value at C5-C6-C11 has the 126.3° match with XRD values 123.7 ° and its minimum value for C1-C2-C3, C13-C12-C14 is 116.18 ° and its match with experimental values 118 °. For CCH, the maximum value is observed at the 117.4 ° in C2-C3-H18 and its experimental value is 120 ° which is well match to the computed value and its minimum value 109.5 ° in C2-C1-H17 also correlated to XRD value is 109.5 ° [24]. For the CCO the maximum and minimum values of the C1-C2-O7, C3-C2-O7 are 121.36 °, 122.44 ° which is corelated to the experimental value 120°, 121°. In CCH bond angle represent the maximum value as 117.3 ° for C2-C3-H18, minimum value as 109.8 ° for C2-C1-H17 correlated to the 120 °,109.5 ° XRD values are well matched to the computed values [25]. For the HCH, the value 110 ° of H16-C1-H17 which is maximum value among these represent the matched XRD value 109 ° and the minimum value 106.8 °of H15-C1-H16 well agreement with the experimental value 107.9 °.

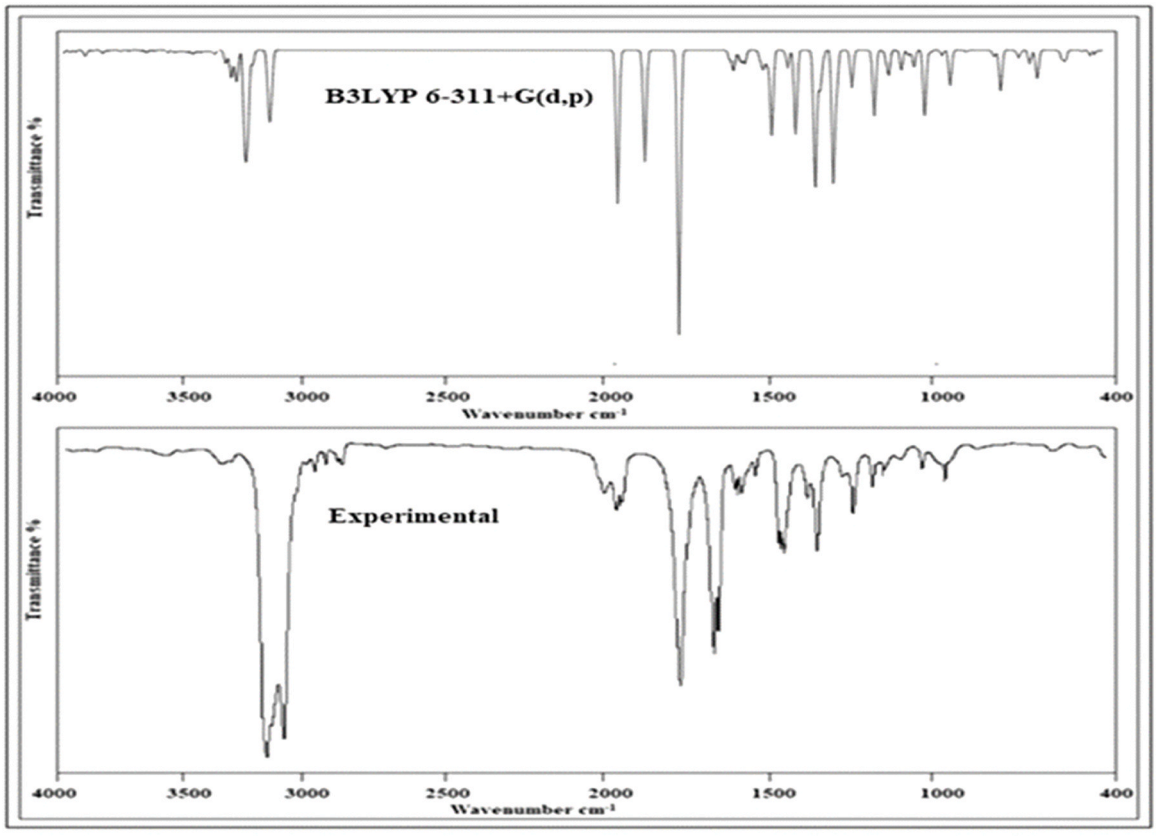

Fig. 5. Experimental and theoretical (B3LYP/6–311 ++G (d, p) of FT-IR for DMO-hexenone.

Table 3
Vibrational wavenumbers of DMO-hexenone for B3LYP/6–311 + + G (d.p).

B3LYP/6–311 + +G(d.p)	FT-IR (cm^{-1})	Vibrational Assignment &PED %
3183	3182	υCH(99)
3168	3168	υCH(99)
3166	3165	υCH(91)
3158	3156	υCH(99)
3042	-	υCH (98)
3150	-	υCH(86)
3149	-	υCH(86)
3125	-	υCH(97)
3123	-	υCH(94)
3121	-	υCH(94)
3116	-	υCH(89)
3115	-	υCH(86)
3111	-	υCH(98)
3100	-	υCH(100)
3051	-	υCH(91)
3048	-	υCH(86)
3040	-	υCH(92)
1788	1762	υOC(79)
1682	1680	υCC(68)
1526	1530	δHCH(65) + τHCCC (12)
1514	-	δHCH(57)
1513	-	δHCH(55)
1509	-	δHCH(71)
1502	-	δHCH(85)
1499	1498	δHCH(71)
1494	1495	δHCH(88)
1489	-	δHCH(85)
1488	1488	δHCH(83)
1478	1477	δHCH(83)
1431	-	δHCH(60)
1430	-	δHCC(39)
1421	-	δHCC(58)
1409	-	δHCC(47)
1395	-	δHCC(46)
1392	-	δHCC(27)
1345	-	δHCC(64)
1321	-	δHCC(41)
1392	-	δHCC(11)
1321	-	δHCC(12)
1259	1250	τHCCC (10)
1245	-	υCC(48)
1237	-	υCC (10) + τHCCC (14)
1204	1204	υOC (10)
1193	-	δHCC (25)
1077	1077	υOC (24)
1052	-	δHCC (29) + τHCCC (11)
1146	-	δHCC(29)
1040	-	δHCC(24)
1032	1032	τHCCC(54)
1017	-	δHCC(41)
993	993	δHCC(25)
970	969	υCC(18)
954	954	δHCC(18)+ υCC(12)
953	-	δHCC(30)+ υCC(21)
921	-	υCC(34)
867	-	τHCCC(19)
841	850	τHCCO(26)+ τHCCC(16)
792	792	υCC(57)
705	-	υCC(22)+ δHCC(21)
685	688	υOC(17)+ υCC(11)
629	-	υCC(18)
595	599	δHCC(30)
577	579	δCCO(34)
571	-	δHCC(30)
495	493	τHCCO(23)
485	475	δHCC(41)$_+$τHCCO(11)
431	429	τHCCO(37)
408	400	δCCC(42)

6.2. The mulliken atomic charges

Quantifying the distribution of electronic density among atoms in a molecule is commonly accomplished by the calculation of atomic charge. The first and most basic technique is the Mulliken atomic charge. It takes into account both the shared electron density in molecular orbitals and the electron density attributed to the atom's own orbitals. For non-magnetic systems, Mulliken population analysis leads to Hirshfeld charges, Hirshfeld bonds, and Mulliken expenses [26]. One can ascertain the effective valence charge by contrasting the formal ionic charge with the Mulliken charge on the anion species. A chemical bond's strength and whether it is covalent or ionic can be determined by its effective valence charge and it is based on the B3LYP-D/6–311 + +G (d, p) theory, a computed effective valences of the atoms listed in Table 2 indicates that among the investigated in gas phases, chemical bonding is demonstrated between the atoms with considerable covalency [27]. The overlap population, which is near zero, suggests that there is little contact across the two atoms' electrical populations, as well as bond with the smallest Mulliken population may be disregarded when determining the hardness of a material. It has been discovered that there is a correlation between low overlap population and high ionicity. Conversely, a high number denotes a high degree of covalency in the chemical interaction. This modifies the vibrational spectrum, which impacts several other attributes of the system, including the dipole moments, electronic structures, polarizability of molecules, atoms' bond lengths, acidity-basicity characteristics, etc. [28]. The donor atoms that function as a nucleophilic charge in DMO-hexenone are C_1, C_4, C_5, C_6, O_7, C_8, C_9, O_{10}, C_{13}, and C_{14}. Although the atoms C_2, C_{11}, and C_{12} possess electrostatic charges. On their acceptor electrons. The significant positive charge of 0.408 a. u of C_2, the positive carbon connected to function as a CO group, indicates the acidic character of this carbon. Thus, in this case, nucleophilic attack is preferable. Additionally, the co-atom-attached C6 exhibits −0.219 a.u negative charges. O_7 and O_{10} oxygen atoms have respective negative charges of 0.47 a.u and 0.49 a.u. Hydrogen has the greatest concentration of positive charges between H_{15} and H_{32}. With intermolecular bonding, H_{32} has the highest positive charge of any hydrogen at 0.134 a.u [29]. It also has a maximum negative charge (-0.47 a. u) at the O_7 location when attacked by electrophiles and the positive atom H_{32} site when attacked by nucleophiles. There may be an electrophilic assault at C_4 (-0.003) a.u, C_5 (-0.026) a. u, and C_3 (-0.143) a.u because to the high electron density at those locations.

6.3. Vibrational assignment

The most significant vibrations, such as CH, CC, OC, CCO, HCCC, HCC, HCH, and HCCO, are displayed in DMO-hexenone's FT-IR spectra Fig. 5. Table 3 tabulates FT-IR wave numbers, both computational and experimental. The IR absorption intensities of DMO-hexenone, as shown in the table, are consistent with the PED results. Gauss View and VEDA software are powerful tools used to analyse and assign vibrational modes in molecular systems, interpret vibrational spectra, apply frequency scaling, and help validate computational methods against experimental data. The vibrational calculations are performed using the gas phase DFT-B3LYP functional with 6–311 + +G (d, p) basis sets [30]. Vibrational frequencies were computed and used to ascertain the normal modes' vibrational assignments. Furthermore, the examination of the vibrational assignments of the DMO-hexenone is conducted by a review of prior research studies' literature. For the linear vibrational assignment, the molecule DMO-hexenone contains32 atoms having C1 point group symmetry and 91 normal modes of vibration. There were 34 torsional bending vibrations, 40 bending vibrations, and 34 stretching vibrations. Normal mode vibrational investigations are used to compare experimental and theoretical wave numbers. For compounds like CH, HCH, HCCC, HCC, CC, OC, CCO, CCC, HCCO, and CCC, vibrational assignments involve recognizing the distinctive vibrations connected to each bond and the overall structure.

6.3.1. CH vibration

It is typically possible to tell whether a structure has one or more aromatic rings based on the C–H bond. The CH bond stretching vibration

Table 4
Theoretical energy parameters of DMO-hexenone molecules.

Electronic properties	Values (eV)	Electronic properties	Values (eV)
E_{HOMO} (eV)	6.11	Chemical hardness	−2.45
E_{LUMO} (eV)	1.21	Chemical softness	−0.408
E_{HOMO}–E_{LUMO} (eV)	4.89	Electrophilicity Index	−5.46
Ionization potential	−6.11	Nucleophilicity Index	−0.18
Electron affinity	−1.21	Electron donor power	−4.87
Electronegativity	−3.66	Electron acceptor power	−1.21
Chemical potential	3.66	ΔN_{MAX} (eV)	−1.49

is usually reported in the C-H stretching region of 2800–3300 cm^{-1} . The region between 3100 and 3300 cm^{-1}It stands out for the prompt identification of C-H stretching vibration, is where the hetero aromatic structure shows the existence of in the gas phase C–H stretching vibration [31]. There are three types of vibrations produced by the substituted molecule like stretching, in-plane, and out-of-plane bending. The substituent's type has no discernible effect on the bands in this area. The calculated C-H stretching vibrations at 3183 cm^{-1}, 3168 cm^{-1}, 3166 cm^{-1}, and 3158 cm^{-1} match the experimental values of 3182 cm^{-1}, 3168 cm^{-1}, 3165 cm^{-1} and 3156 cm^{-1}, with PED values of 99 %, 99 %, 91 % and 99 % respectively. This agreement validates the dependability of the theoretical model utilized DFT/B3LYP/6–311 + +G (d, p).

6.3.2. CH_2 vibration

The CH2 vibration mode in the Methylene Group (H-C-H) is typically observed between 1400 and 1500 cm^{-1} [32]. The predicted frequencies of 1526cm-1, 1499cm-1, 1494cm-1, 1488cm-1 and 1478cm-1 are consistent with experimental values 1530cm-1, 1498cm-1, 1495cm-1, 1488cm-1 and high PED values support these assignments.

6.3.3. HCCC, HCC vibration

The bending modes of the C-H bond in HCCC torsion and HCC bending are often found in the 600–900 cm^{-1} range [33]. The calculated HCCC values of 1526 cm^{-1} , 1259 cm^{-1} , and 841 cm^{-1} are correlated with the experimental values of 1530 cm^{-1} , 1250 cm^{-1} , and 850 cm^{-1} to get the PED values of 65 %, 10 %, and 16 %. The observed wave numbers for HCC are 993 cm^{-1} , 954 cm^{-1} , 595 cm^{-1} , and 485 cm^{-1} . These correspond to the experimental wave numbers of 993 cm^{-1} , 599 cm^{-1} , 475 cm^{-1} , and the PED values of 25 %, 18 %, 30 %, and 41 %.

6.3.4. CC, CCC vibration

An σ-bond, C-C stretching vibration is commonly recorded in the 800–1200 cm^{-3} range. Stretching in π-bond, C═C stretching vibration often expresses itself between 1500 and 1700 cm^{-1} . Particularly in linear or cyclic structures, the CCC (carbon-carbon-carbon) group's vibrational modes involve a variety of stretching and bending vibrations connected to the carbon-carbon bonds. Because of the ring strain and angle bending, the torsional bending mode is particularly important in cyclic compounds [34]. Among the 68 %, 18 %, and 12 % PED Values, the CC stretching vibrational achieves 1682 cm^{-1} , 970 cm^{-1} , and 954 cm^{-1} with experimental values of 1680, 969, and 954. The computed value of 408 cm^{-1} in CCC Bending vibration is associated with the 400 cm^{-1} with 42 % PED values.

6.3.5. OC, CCO, HCCO vibration

The stretching vibration of the carbon-oxygen single bond (C-O) usually occurs within the lower frequency range of 1000–1300 cm^{-1} . Outside the plane Bending modes are caused by the CCC bond angle moving out of the plane that the other two carbons form when one carbon travels out of it. These modes usually have frequencies in the 400–700 cm^{-1} range [35]. Bending Modes of H-C-C and C-C═O the vibrations caused by bending linked to the H-C-C and C-C═O bonds usually transpire at reduced frequencies, generally falling between 600 and 1200 cm^{-1} . Since HCCO is a radical species, its vibrational spectrum may deviate slightly from that of stable molecules because of the unpaired electron and unique electrical structure, which may induce frequency shifts. Infrared spectroscopy and computational approaches are typically used to study these modes. In the case of OC stretching vibration, the experimental values from FT-IR spectra correspond to 1204 cm^{-1} , 1077 cm^{-1} , and 685 cm^{-1} , along with PED values of 10 %, 24 %, and 17 %. For CCO bending vibrational 577 cm^{-1} , 34 % of PED values are labelled with experimental value 579 cm^{-1} .The band is located in the torsional vibration zone of the HCCO at 841 cm^{-1}, 485 cm^{-1} , 495 cm^{-1} , 431 cm^{-1} , and 850 cm^{-1} . The PED values of 26 %, 11 %, 23 %, and 37 % are in relation to the experimental values of 475 cm^{-1} , 493 cm^{-1} , and 429 cm^{-1} .

6.3.6. Carbonyl (C═O) vibration

The carbonyl stretching frequency have been assigned region from 1700 to 1800 cm^{-1} found from literature review of carbonyl based compounds [36]. In our study, the experimental FT-IR spectrum of C═O oscillation shows area at 1762 cm^{-1} as a strong band (maximum intensity) and the computational estimated C═O vibration allocated peak at 1788 cm^{-1} with 78 % PED contribution. Both the experimental and theoretical frequency of band C═O have been correlated in a good agreement successfully.

6.4. The reactivity and chemical stability of DMO-hexenone compounds

The chemical stability and reactivity of DMO-hexenone molecules were investigated using the Frontier Molecular Orbital theory, which is fundamental to chemical reactions. The FMO characteristics of the DMO-hexenone molecule were determined utilizing a 6–311 + +G (d, p) basis set and DFT/B3LYP [37]. The energy gap, HOMO, LUMO, and a molecule's chemical stability and reactivity are all covered by the FMO theory. DMO-hexenone molecules have a HOMO-LUMO energy gap. Whereas LUMO denotes obtaining the electron inside the molecule, HOMO denotes donating the electron [38]. The EHOMO-ELUMO gap indicates the energy difference between the HOMO and LUMO orbitals. This gap provides information into molecules stability and reactivity. A narrower gap often indicates more chemical reactivity. High stability is shown by title compound's HOMO value of 6.11 eV, LUMO value of 1.29 eV, and maximal electronic transition energy gap of 4.89 eV. Softness (-0.408 eV-1) is associated with the molecular orbital's greater stability state, whereas hardness (-2.45 eV) is associated with the molecular orbital's lower state. The title compound has a chemical electronegativity value of −3.66 eV, indicating high reactivity and inhibitory effectiveness [39]. Electron affinity and ionization potential are represented by the HOMO and LUMO. Electrophilicity has a donor of −5.46 eV and nucleophilicity has an acceptor of −0.18 eV^{-1}. With an additional electronic charge of −1.49 eV, DMO-hexenone molecules exhibit an improved level of reactivity. Table 4 provides a thorough overview of the theoretical energy parameters, and Fig. 6 shows the HOMO-LUMO energy gap, which gives a visual depiction of the stability and electronic transitions of the molecule.

Theoretical Energy Parameters Calculation of DMO-hexenone

$$E_{HOMO} = 6.11eV \quad (1)$$

$$E_{LUMO} = 1.21eV \quad (2)$$

Ionization Potential

Ionization Potential (IP) = − E_{HOMO}

Substituting Eq. 1

$$\text{Ionization Potential (IP)} = \text{-}6.11eV \quad (3)$$

Electronic Affinity

Electronic Affinity (EA) = -E_{LUMO}

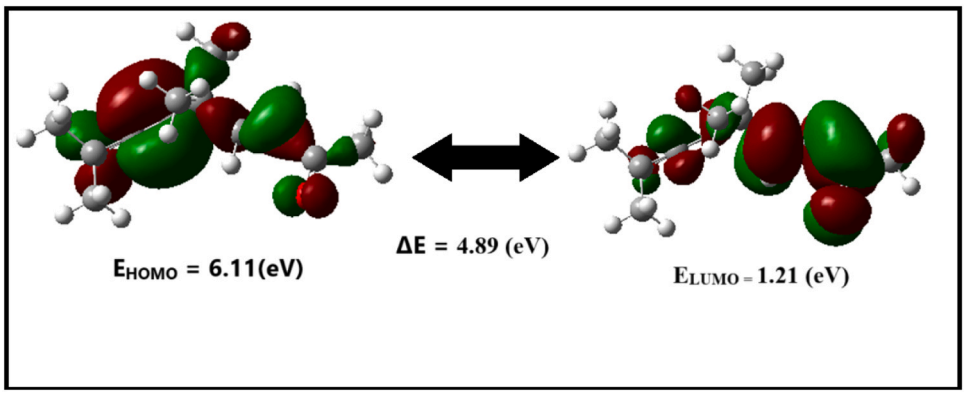

Fig. 6. HOMO-LUMO energy gap of DMO-hexenone molecules.

Substituting Eq. 2

$$\text{Electronic Affinity (EA)} = -1.21\text{eV} \tag{4}$$

Substituting Eqs. 3 and 4

$$E_{HUMO} - E_{LUMO} = 4.89\ \text{eV} \tag{5}$$

Electronegativity

$$\text{Electronegativity}(\chi) = \frac{IP + EP}{2} \tag{6}$$

$$= \frac{(-E\ HOMO - E\ LUMO)}{2}$$

$$= \frac{[(-6.11) + (-1.21)]}{2}$$

$$\text{Electronegativity } (\chi) = -3.66\text{eV} \tag{7}$$

Electronegativity (χ) = − Chemical Potential (μ)

$$\text{Chemical Potential } (\mu) = 3.66\text{eV} \tag{8}$$

Chemical Hardness

$$\text{Chemical hardness}(\eta) = \frac{IP - EP}{2} \tag{9}$$

$$= \frac{(-E\ HOMO + E\ LUMO)}{2}$$

Substituting Eqs. 3 and 4

$$= \frac{-6.11 + 1.21}{2}$$

$$\text{Chemical hardness } (\eta) = -2.45\text{eV} \tag{10}$$

Chemical Softness

$$\text{Chemical Softness}(\sigma) = \frac{1}{\eta} \tag{11}$$

Substituting Eq. 10

$$= -0.408\text{eV}^{-1} \tag{12}$$

Electrophilicity index

$$\text{Electrophilicity Index}(\omega) = \frac{\mu 2}{\eta} \tag{13}$$

$$= \frac{(3.66)^2}{(-2.45)}$$

$$= \frac{13.39}{(-2.45)}$$

$$\text{Electrophilicity Index } (\omega) = -5.46\ \text{Ev} \tag{14}$$

Nucleophilicity N index

$$\text{Nucleophilicity N index} = \frac{1}{\omega} \tag{15}$$

Substituting Eq. 14

$$= \frac{1}{(-5.46)}$$

$$\text{Nucleophilicity N index} = -0.18\text{eV}^{-1} \tag{16}$$

Electron Acceptor Power

$$\text{Electron Acceptor Power}(\omega' +) = \frac{(IP + 3EA)^2}{16(IP - EA)} \tag{17}$$

Substituting Eqs. 3 and 4.

$$= \frac{[(6.11 + 3(1.21)]^2}{16(6.11 - 1.21)}$$

$$= \frac{94.86}{-78.24}$$

$$\text{Electron Acceptor Power } (\omega'^{+}) = -1.21\text{eV} \tag{18}$$

Electron Donor Power

$$\text{Electron Donor Power}(\omega' -) = \frac{(3IP + EA)^2}{16(IP - EA)} \tag{19}$$

Substituting Eqs. 3 and 4.

$$= \frac{[3(-6.11) + (-1.21)]^2}{16(-4.89)}$$

$$= \frac{381.81}{-78.24}$$

$$\text{Electron Donor Power } (\omega'^{-}) = -4.87\text{eV} \tag{20}$$

Additional Electronic Charge

$$\text{Additional Electronic Charge}\Delta N_{max} = \frac{\mu}{\eta}$$

$$= \frac{3.66}{-2.45}$$

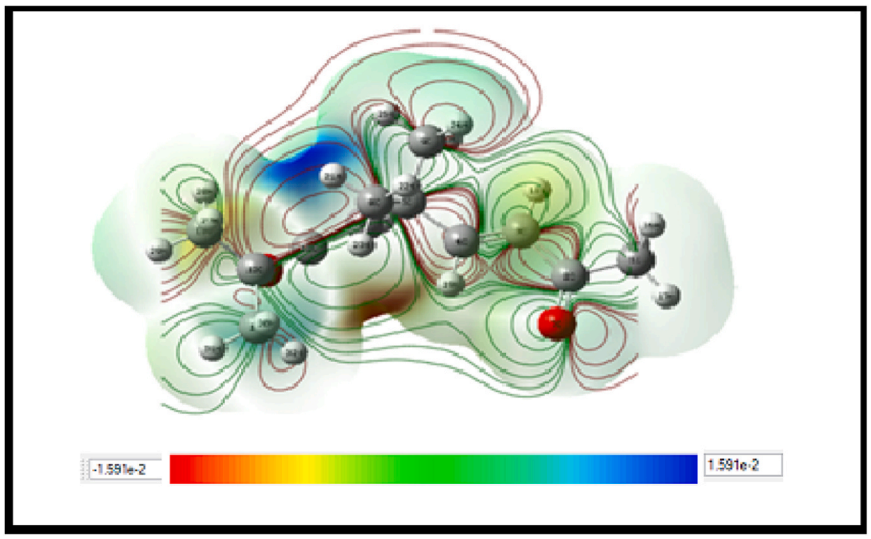

Fig. 7. MEP map surface on DMO-hexenone molecules.

Table 5
Natural bond orbital analysis DMO-hexenone.

Donor NBO (i)	Acceptor NBO (j)	E(2)[a] Kcal/mol	E(j)-E(i)[b] a.u	F(i, j)[c] a.u
(π) $C_2 – O_7$	(π*) $C_3 – C_4$	6.83	0.40	0.047
LP (2) O_{10}	(σ*) $C_{12} – C_{14}$	7.43	0.70	0.067
(σ) $C_6 – H_{20}$	(σ*) $C_{11} – C_{12}$	7.62	0.87	0.073
(σ) $C_{14} – H_{30}$	(σ*) C_{13} - H_{27}	9.61	0.97	0.087
(σ) $C_{13} – H_{27}$	(σ*) $C_{14} – H_{30}$	10.12	0.96	0.088
(σ) $O_{10} – C_{12}$	(σ*) $C_6 – C_{11}$	14.71	1.40	0.128
LP (2) O_7	(σ*) $C_2 – C_3$	16.25	0.88	0.108
LP (2) O_7	(σ*) $C_1 – C_2$	22.39	0.65	0.109
LP (2) O_{10}	(σ*) $C_6 – C_{11}$	25.72	0.36	0.087
(π) $C_3 – C_4$	(π*) $C_2 – O_7$	33.54	0.31	0.092

[a] E (2) means energy of hyper conjugative interaction (stabilization energy).
[b] Energy difference between donor and acceptor i and j NBO orbitals.
[c] F (i, j) is the fork matrix element between i and j NBO orbitals.

Additional Electronic Charge $\Delta N_{max} = -1.49eV$ (21)

6.5. Molecular electronic potential

Molecular electrostatic potential determines the magnitude of nearby charges at a certain location, such as electrons and nuclei [40]. To predict electrophilic and nucleophilic attack sites on the DMO-hexenone molecule B3LYP/6–311 + +G (d, p), an optimized geometry, was used to calculate MEP. The electrophilic regions (positive potential) indicates that these places are electron deficient and will attract nucleophiles (electron rich species). Nucleophilic zones (negative potential) are places that are electron rich and susceptible to assault by electrophiles (electron-deficient species). These reactive spots where chemical interactions, such as nucleophilic or electrophilic assaults would occur, resulting in reaction such as substitution, bonding, or proton transfer, all of which are required for the molecule's reactivity and biological activity [41].Colours show different electrostatic potential values at the surface. Potential increases from red to orange to yellow to green to blue. In combination, these maps have colour codes ranging from −1.591e-2 a.u. (deepest red) to 1.591e-2 a.u. (deepest blue). Fig. 7 illustrates that the positive (white) and negative (red) portions of MEP correspond to electrophilic and nucleophilic reactivity, respectively [42]. The MEP successfully discovered reactivity sites for both intra- and intermolecular interactions. In gases and solvents, oxygen in contrast to hydrogen atoms, which have a positive electrostatic potential and a nucleophilic reactive site (acceptor), atoms have a negative electrostatic potential, indicating an electrophilic reactive site (donor). Green surface area indicates a localized zero electrostatic potential. As with other solvents, the reactive sites of DMO-hexenone molecules exhibit both gas and water phases, which are related with biological activity [43]. The reactive portions of the molecule can be recognized by electron and proton interactions, indicating biological activity.

6.6. Natural bonding orbital (NBO) analysis

The Inherent Connection a wave function's orbital analysis is the first prerequisite for establishing communication between designated electronic structure systems. This method effectively analyses and identifies the Energy and Bonds associated with just one pair of electrons that is crucial for physiochemical processes [44]. This technique promoted hyper conjugative effects, hydrogen bonds between donor and acceptor molecules, and electronic interactions. The interaction energy between donor and acceptor electrons and the stability of these orbital connections can both be assessed using the energy gap between interacting orbitals. It is feasible to determine the most stable connection by computing the second-order stabilization energy E2.

$$E^{(2)} = \Delta E_{ij} = q_i \frac{F(i,j)^2}{\varepsilon_j - \varepsilon_i}$$

Here, qi is the occupancy of the εi orbital, $F(i, j)$ is the off-diagonal component of the Fock matrix, and εi and εj stand for the diagonal elements of orbital energies. The size of E (2) is directly proportional to the strength of the interaction between the donor and acceptor electrons. A greater interaction between the two is indicated by a higher value of (2). Table 5 presents computed DMO-hexenone findings [45]. The bonding pairs (donor) were projected to have a higher stabilizing energy E (2) value while the DMO-hexenone molecule is interacting intramolecularly by hyper conjugation. Atoms in (π) C_2-C_7 to (π*) C_3-C_4 anti bonding orbitals have a stabilization energy of 0.40 kJ/mol, whereas those in (π) C_3-C_4 to (π*) C_2-C_7 have a stabilization value of 0.31 kj/mol. The interaction between (σ) C_6-H_{20} and σ* (C_{11}-C_{12}) has a stabilizing energy of 0.87 kJ/mol. Likewise, the stabilization energy of the interaction between σ (O_{10}-C_{12}) and σ* (C_6-C_{11}) is 1.40 kJ/mol. An energy transfer of 0.70 kJ/mol is obtained from the lone pair (LP) (2) of O_{10} to σ* (C_{12}-C_{14}). Similarly, a stabilization energy of 0.88 kJ/mol is obtained via electron donation from the lone pair (2) of O_7 to σ* (C_2-C_3). The interaction that stabilize the system the most are LP (2) O_{10} to σ*

Table 6
Electronic excitations of 3MBD – TMC obtained by TD-DFT/B3LYP/6–311 + +G (d, p) methods.

Solvent state	Absorption band λ max (nm)	Energy cm-1	Oscillation Strength (f)	Band gap eV	Major Contributions Energy (%)
Gas	386.29	25887.17	0.0	0.5426	H−1->LUMO (97 %)
	359.08	27848.71	0.0003	1.6471	HOMO->LUMO (98 %)
	278.04	35965.87	0.0375	3.0063	HOMO->L+ 1 (96 %)

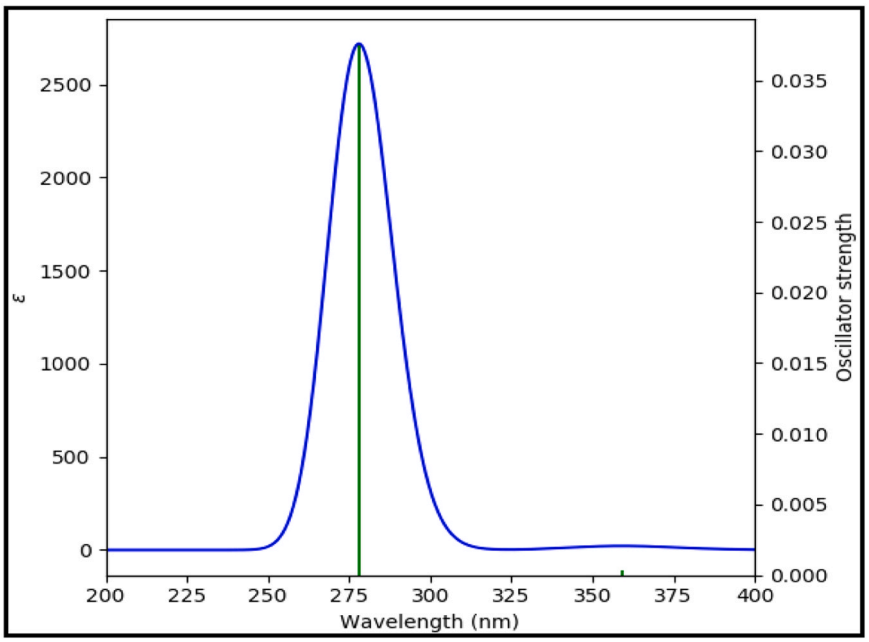

Fig. 8. UV Spectrum of DMO-Hexenone.

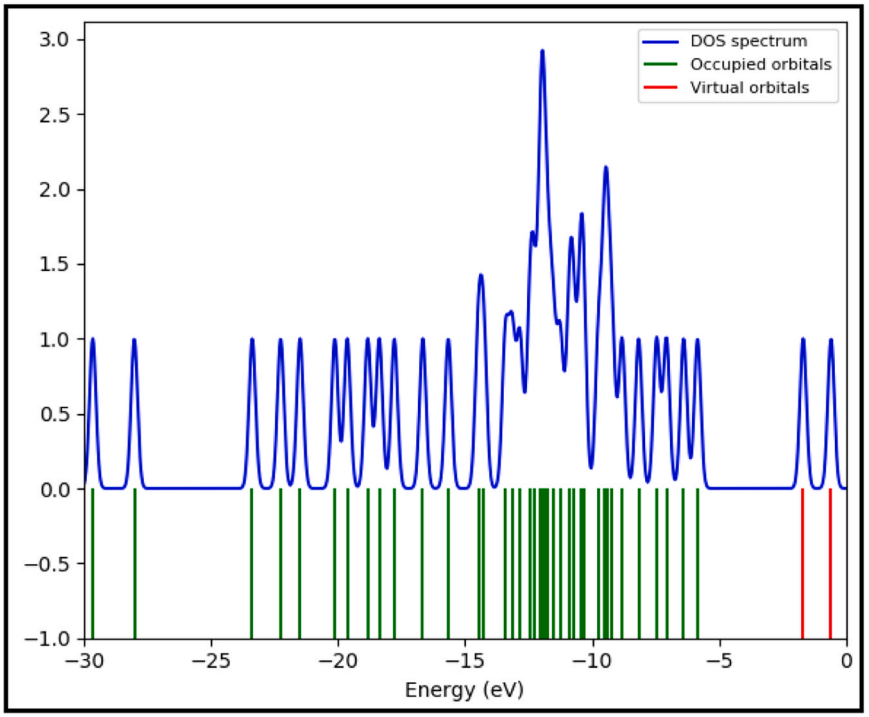

Fig. 9. DOS Spectrum of DMO-Hexenone.

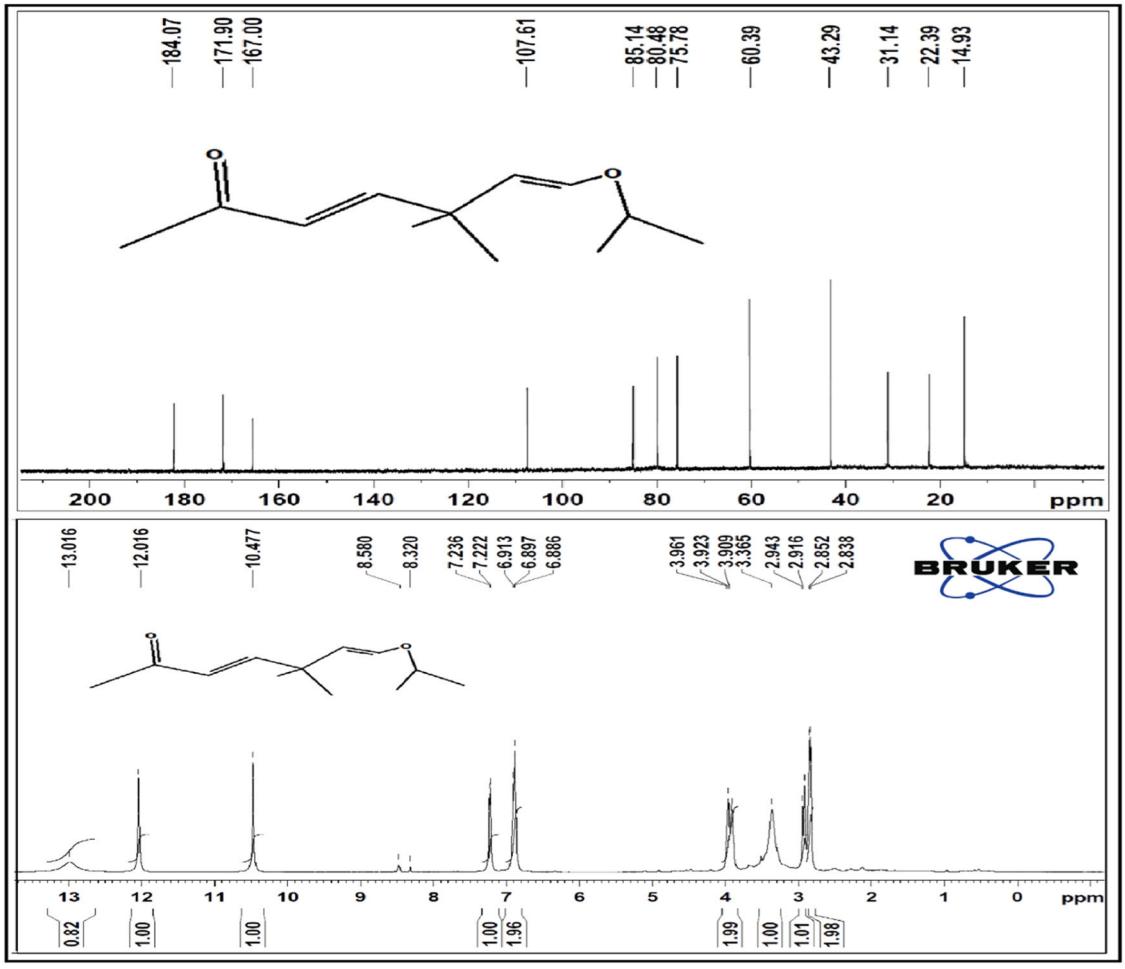

Fig. 10. ^{1}H and ^{13}C NMR spectrum of DMO-Hexenone.

Table 7
of ^{1}H and ^{13}C NMR Analysis.

Atom	Theoretical Chemical Shift in ppm	Experimental chemical shift in ppm	Atom	Theoretical Chemical Shift in ppm	Experimental chemical shift in ppm
C_5	14.8109	14.93	H_{28}	5.5094	2.943
C_8	23.8079	22.39	H_{26}	5.6328	3.365
C_1	31.5064	31.14	H_{24}	5.9863	3.909
C_9	41.1987	43.29	H_{16}	6.2829	3.923
C_{14}	67.8763	60.39	H_{17}	6.3535	3.961
C_{12}	73.0859	75.78	H_{22}	6.5249	6.886
C_6	79.1388	80.48	H_{19}	7.2322	6.897
C_{13}	82.4275	85.14	H_{29}	7.3595	6.913
C_3	109.8191	107.61	H_{23}	7.4269	7.222
C_2	162.7753	167.00	H_{21}	7.6787	7.236
C_{11}	176.1426	171.90	H_{32}	8.0798	8.320
C_4	183.1847	184.07	H_{31}	8.7025	8.580
H_{20}	3.6342	2.838	H_{18}	12.0189	10.47
H_{15}	3.9474	2.852	H_{27}	13.0758	12.00
H_{25}	4.1215	2.916	H_{30}	14.5575	13.016

(C_6-C_{11}) (25.72 kcal/mol), LP (2) O_7 to σ* (C_1-C_2) (22.39 kcal/mol) and π (C_3-C_4) to π* (C_2-O_7) (33.54 kcal/mol). These interactions indicate high electron donation from lone pairs on oxygen atoms to anti-bonding orbitals which greatly contribute to system stability [46].

6.7. UV -visible analysis

The chemical's visible and ultraviolet spectrum with the DMO-hexenone was experimentally recorded using several solvents, including gas, and is measured in the 200–300 nm region. Table 6 **and** Fig. 8 show the results. With B3LYP/6–311 + +G (d, p) and TD-DFT approach, DFT was used to analyze the molecule's UV–visible (UV-Vis) spectrum. Three significant excited states were found by the computational findings; these states were distinguished by distinct oscillator strengths, excitation energy, absorption bands, and important electronic transitions [47]. Fig. 9 determines the group contributions to the molecular orbitals to create the density of the state (DOS) using the Gauss-Sum 2.2 Program. Comparable transitions with equal contributions are seen in the gas phase at three states: 386.29 nm, 359.08 nm, and 278.04 nm. These wavelengths are associated with specific

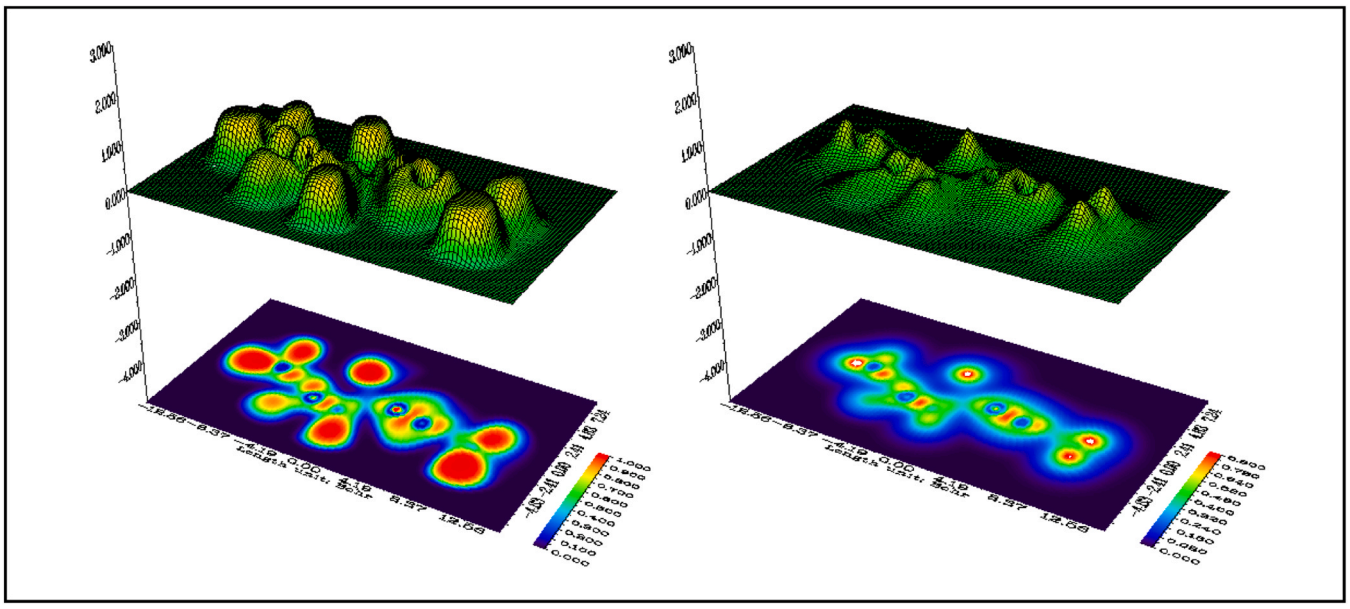

Fig. 11. ELF and LOL of the DMO-hexenone molecule.

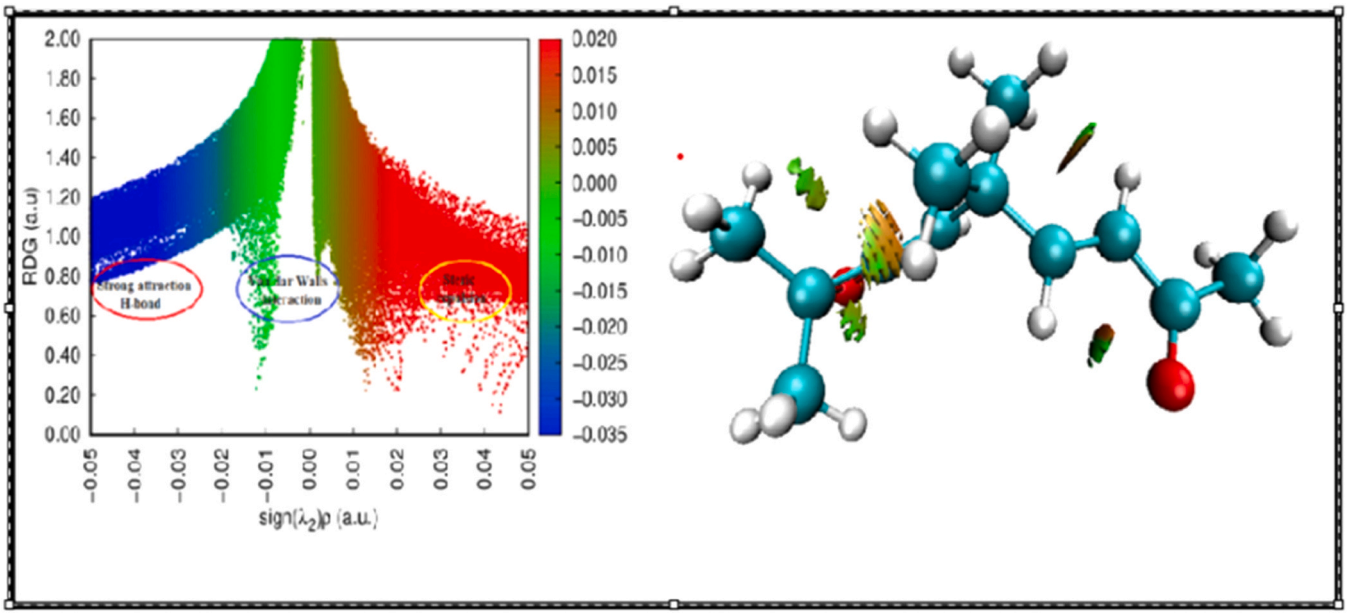

Fig. 12. Reduced density gradient (RDG) analysis and Non -covalent interaction (NCI) scatter diagram of DMO-hexenone.

Table 8
Active site, hydrogen bond and docking with anti-cancer receptor targets.

Protein (PDB ID)	Bonded residues	No. of hydrogen bond	Bond distance (Å)	Estimated Inhibition Constant (μm)	Binding energy (kcal/mol)	Reference RMSD (Å)
1DAF	MET 4 (O…HN) TRP 47 (O…2HD2)	2	2.1 1.8	65.13	−5.71	64.74

molecular orbital transitions that involve both π→π* and n→π* transitions [48]. With a 97 % contribution at the S1 state absorption wavelength, at λmax = 386.29 nm, the maximum absorption wavelength is correlated with the change from HOMO-1 to LUMO, confirming an n→π* transition. This transition includes the excitation of a non-bonding electron (n) from the HOMO-1 orbital to the anti-bonding LUMO (π*), possibly from lone pairs on electronegative atoms, resulting in a low energy transition. Whereas the second (S2) and third (S3) excited state at λmax is 359.08 nm and 278.04 nm respectively. In the S2 transition corresponds to the excitation of an electron from the bonding π orbital (HOMO) to the anti-bonding π* orbital (LUMO) with a contribution of 98 %. The S3 state shows a transition that involves excitation of an

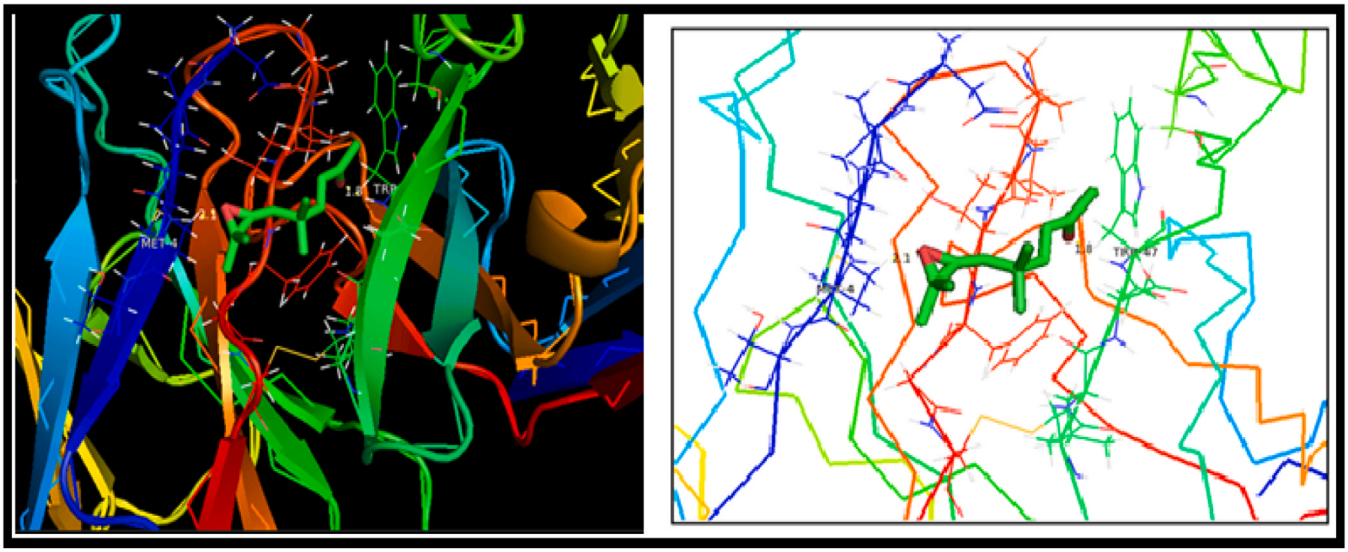

Fig. 13. The ribbon form represents the protein (1DAF) and ligand docking complex at the active site MET 4 and TRP 47 amino acids.

electron from the HOMO to the higher anti-bonding π* orbital (LUMO+1) having a 96 % contribution. The type of transition at both S2 and S3 state at λmax is π→π* transition [49]. A chemical system's distribution of occupied orbitals and energy levels can be inferred from the density of states (DOS) spectrum. The virtual orbital (LUMO) in the title compound is red, which indicates a positive charge, and the occupied orbital (HOMO), which is green, indicates a negative charge in the donor molecule. While the compound's homo had a wide range of electrons to reach the stable state, the stable state was formed via nucleophilicity.

6.8. ^{1}H and ^{13}C NMR analysis

One of the most crucial methods for characterizing the structural conformation of organic molecules is NMR spectroscopy. Since 1H and 13 C NMR are popular and useful methods for revealing more details about the molecule under investigation, we employed them. The foundation set 6–311 + +G (d, p) was utilized to calculate theoretical 1H and 13 C chemical shifts [50]. One of the most popular methods for figuring out isotropic nuclear magnetic shielding tensors is the GIAO approach to predict the chemical environments of individual atoms [51,52]. Important structural characteristics based on these theoretical shifts are provided by the 1H and 13 C NMR spectra graphs, Fig. 10, which indicate the distribution of chemical shifts for the protons and carbons in DMO-hexenone. A range of carbon locations impacted by different functional groups may be seen in the 13 C NMR chemical shifts, ranging from 14.81 ppm for C5 to 183.18 ppm for C4. Lower shift carbons, like C4, are in more electron-rich (shielded) places, whereas higher shift carbons, like C1, experience enhanced de-shielding, often because of nearby electron-withdrawing groups. This wide range demonstrates the influence of electrical factors, such as proximity to groups that contribute or remove of electrons. The accompanying graphs for the 1H and 13 C NMR spectra, which display peaks that correspond to the calculated chemical shift values in Table 7, clearly confirm these findings. The Carbon (C4) peak at 183.18 ppm represents methylene, it is joined to the remainder of the molecule by a double bond between carbons. The C1 methylene group is at 41.19 / 43.29 ppm, while the CO functional group is at C2, which is at 162.77 / 167 ppm. The measured theoretical chemical shift of 1H falls between 3.6342 and 14.557 ppm. The compound DMO-hexenone 1H and 13 C NMR spectra are displayed in Fig. 10. The CH2, CH3 group is in charge of the larger chemical shift as it has a stronger electronegative atom connected. The double bonds C═C and C═O in DMO-hexenone are represented by the largest ppm values in the peaks and their corresponding values of the C-H chemical shift in DMO-hexenone —H20 with 3.6 / 2.9 ppm, H15 with 3.9 / 2.9 ppm, H16 with 6.3 / 6.8 ppm, and H17 with 6.326 / 6.89 ppm. The specific atom that corresponds to the chemical shifts are C_6, C_5, C_8, C_1, C_9, C_4 carbon shifts and H_{15}, H_{19}, H_{20}, H_{22}, H_{23}, H_{21}, H_{27}, $H3_0$, H_{31}, H_{32} were correlated. Their presence is confirmed by the calculated chemical shift and experimental NMR values of the methylene and methyl, CO groups, respectively with corresponding experimental values matched to the theoretical values of the title compound DMO-hexenone.

6.9. Analysis of LOL and ELF

The function of electron localization (ELF) is a quantum chemistry technique that identifies regions with high electron density, showing where electrons are most localized in a molecule. It facilitates the identification of lone pairs and bonding interactions. The Localized Orbital Locator (LOL) adds to this by examining the spatial contributions of individual orbitals to electron density, indicating where particular orbitals influence electron distribution. ELF and LOL work together to offer information about the bonding characteristics and electrical structure of molecular systems. Using the Multiwfn application, we obtain ELF and LOL. They both share comparable chemical compositions because they reflect kinetic energy concentrations [53]. Fig. 11 displays the localized orbital locator and electron localized function contour and colour-shaded maps. The colour markers range from blue to red, signifying the 0.0–1.0 scale ranges for LOL and ELF images. LOL has a range scale, as does ELF, with the bonding and nonbonding localized electronic regions ranging from 0.5 to 1.0. The electronic region below 0.5 is considered delocalized. Furthermore, According to the LOL maps, electronic localization fuelled by electron density greater than 0.5 yields the highest values. The red area indicates the covalent region's high LOL value, whereas the blue circular region encircling the nuclei represents the electron depletion zone between the outer and inner shells [54]. The title compound's ELF values are characterized using two-dimensional graphical data with color grading. The lower end of the ELF spectrum is shown by blue, while high ELF levels are indicated by red. Single electrons in the title compound are shown in red, indicating the highest Pauli repulsion near hydrogen. Zones of electron depletion are highlighted by the blue spots, which are located close to nitrogen and chlorine and contain electrons with similar spins. ELF and LOL analyses provide important information on reactivity, molecular bonding, and chemical structure; their use in the quantitative evaluation of aromaticity is especially highlighted [55].

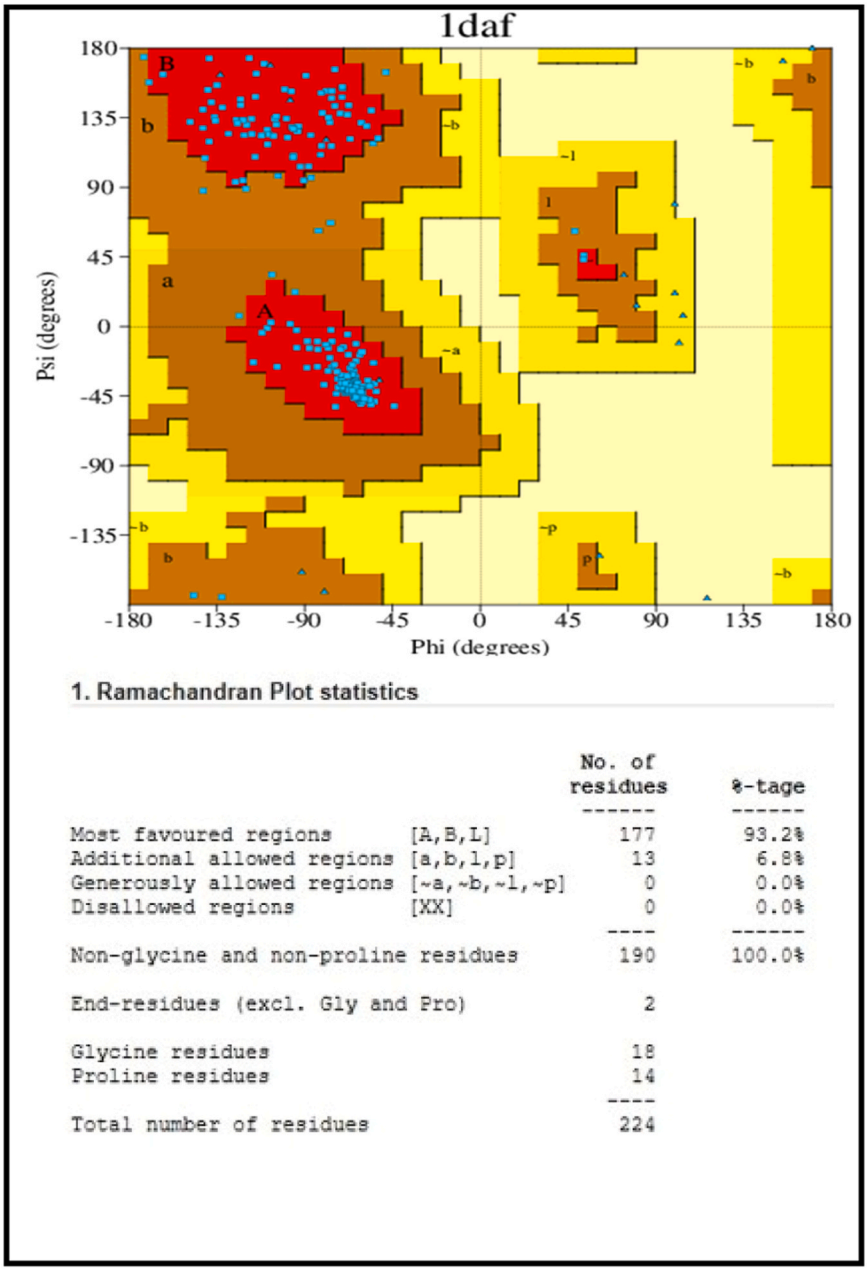

1. Ramachandran Plot statistics

		No. of residues	%-tage
Most favoured regions	[A,B,L]	177	93.2%
Additional allowed regions	[a,b,l,p]	13	6.8%
Generously allowed regions	[~a,~b,~l,~p]	0	0.0%
Disallowed regions	[XX]	0	0.0%
Non-glycine and non-proline residues		190	100.0%
End-residues (excl. Gly and Pro)		2	
Glycine residues		18	
Proline residues		14	
Total number of residues		224	

Fig. 14. Ramachandran plot for 1taf.

6.10. *Analysis of RDG*

The Gradient of Reduced Density (RDG) is a method used in computational chemistry to investigate fluctuations in electron density within molecules. RDG identifies regions of interest, such as bonding or non-bonding interactions, by evaluating how electron density varies, revealing information about molecule structure and function. The low density gradient identifies weak interactions. The bottom and upper electron regions evaluate the system's low density and high density gradient, as well as weak and strong interactions [56]. Bonded interactions ($\lambda 2 > 0$) and non-bonded interactions ($\lambda 2 < 0$) are distinguished by the sign of $\lambda 2$, the second eigenvalue of the electron density Hessian matrix. These spikes fall into three categories: (i) a large negative value of ($\lambda 2$) ρ; (ii) a large positive value of ($\lambda 2$) ρ, which indicates weak interactions like van der Waals forces or strong steric repulsion; and (iii) values near zero, which indicate non-bonding interactions [57]. RDG parameter's electron density value, $\rho(r)$, represents electron density in the graph, while ($\lambda 2$) ρ depicts the RDG map's contrast between attraction and repulsion. According to the RDG graph, the red color range and strong steric effect repulsion are shown when ($\lambda 2$) ρ is larger than 0, which can be a key factor in the molecule's overall stability. This zone shows where atoms are too near for efficient bonding or contact due to high repulsive forces. when ($\lambda 2$)ρ is less than 0, it indicates that the areas in the molecule have attractive interactions and the green color and van der Waals interactions are considered when ($\lambda 2$)ρ is near 0 [58]. In locations with ($\lambda 2$) $\rho > 0$, we see ρ values ranging from 0.05 to 0.10 e/ Å^3 , or even higher. These are locations with a strong electron density gradient, which indicates repulsive interactions. In ($\lambda 2$) $\rho < 0$, electron density is lower than in repulsive areas, and ($\lambda 2$) ρ is negative. Here, we see values of $\rho = 0.03$–0.05 e/ Å^3 , indicating weak but persistent attractive contacts such as Van der Waals forces between nearby atoms. The present analysis used Multiwfn 3.7 and VMD programs to create a 2D scatter plot and RDG isosurface, as illustrated in Fig. 12.

6.11. Analysis of molecular docking

The process of designing drugs based on structure is called molecular docking which simulates receptor-ligand interactions and predicts binding modes and affinities. This could enhance therapeutic target prediction and provide insight into molecular mechanisms for drug design [59]. AutoDock method 1.5.6 software generates a three-dimensional docking structure for investigation [60]. In the current study, the effectiveness of the DMO-hexenone ligand against renal cell cancer (c-Met inhibitor) was evaluated by synthesizing it and examining its interaction with the transferase active receptor protein 1DAF. Using the Molview.org tool, which made it easier to convert PDB database entries, the ligand—which was identified as 6-(3, 3-dimethyl-oxiran-2-ylidene)-5, 5-dimethyl-hex-3-en-2-one—was created. The RCSB database provided the protein structure needed for docking analysis as a PDB file [61,62]. The DMO-hexenone showed the ligand-protein interaction with the negative binding energy of −5.71 kcal/mol. On comparing a reference drug or known inhibitor establish a standard for comparison. In Robert Roskoski Jr (2024) study [63], Crizotinib, a well-known c-Met inhibitor, has greater binding energies ranging from −7.0 to −8.0 kcal/mol. Including crizotinib as a reference in future research would help us to better understand the efficacy of DMO-hexenone (-5.71 kcal/mol) against renal cell carcinoma. The binding residues are listed in Table 8 of 1DAF, including MET 4 (O…HN) and TRP 47 (O…2HD2). The inhibition constant is predicted to be 65.13 μm, while the reference RMSD value is 64.74 Å [64]. The hydrophobic core of a protein includes MET 4 residues. MET residues favour binding locations over a protein's surface. This could be as a result of MET's strong polarizability and ability to generate hydrogen bonds. Only as a hydrogen bond acceptor can MET sulfur function. Tyrosine residues and TRP are particularly important for securing membrane proteins to the cell membrane. TRP shields delicate hydrogen bonds from moisture. In MET 4 and TRP 47, the amino acid residue number indicates where that specific amino acid is located in the linear chain [65,66]. In a molecule, the average distance between the nuclei of two bound atoms is called the bond distance (or bond length). This characteristic of a link between two fixed-type atoms can be transferred. As illustrated in Fig. 13, the title compounds exhibit a good inhibitor of the 1DAF receptor with two hydrogen bond distance values of 2.1 and 1.8 Å against COLON cancer, and the aforementioned values imply a good docking score. The binding energy of DMO-hexenone (-5.71) is modest when compared to other known anticancer drugs such as Crizotinib (-7.0 kcal/mol or lower). Although lower, this number nevertheless indicates a substantial contact with the receptor implying, possible biological activity. Studies such as Tehmina Akram, Muhammad Athar Abbasi., et al. (2019) [67] have successfully used MD simulations and MM-GBSA computations to validate docking results. By applying these approaches to the DMO-hexenone complex with 1daf, one may learn about the ligand's stability inside the binding pocket and acquire more precise binding free energy estimations, which may differ from initial docking scores owing to solvent and entropic effects. The Ramachandran plot can be used to assess the stability of protein molecules. Furthermore, it provides information that can be utilized to identify, predict, or confirm protein structures. Protein dihedral angles are illustrated on a two-dimensional plane in various spots where stable conformations are known to exist along the protein's backbone [68,69]. The Ramachandran plots for protein 1daf are presented in Fig. 14. This demonstrates that the protein contains 177 residues in allowed locations, which is more than 90 %. Furthermore, the protein contains a large number of residues. Additionally, the protein lacks residues in forbidden areas. There were 224 residues in 1TAF. This may differ depending on the number of residues in each molecule.

7. Conclusion

The compound, DMO-hexenone ($C_{12}H_{18}O_2$), was confirmed by GC-MS analysis. The optimized molecular geometry of DMO-hexenone, calculated using the DFT/B3LYP technique with the 6–311 + +G (d, p) basis set, closely matched experimental XRD data. Key bonds, such as C_2-O_7 and C_6-C_{11}-O_{10}, revealed the existence of carbonyl groups, with CC, CH, and CO bond lengths and angles agreeing well with experimental values. The estimated bond angles for CCC, CCH, CCO, and HCH combinations matched XRD data, demonstrating the computational model's correctness. The Mulliken population analysis found that key nucleophilic donor atoms such as C_1, C_4, C_5, C_6, O_7, and O_{10} have negative charges, whereas electropositive atoms such as C_2, H_{15}, and H_{32} are susceptible to electrophilic and nucleophilic assaults, respectively. The measured FT-IR spectra and the predicted vibrational assignment with PED% were found to be well matched. DMO-hexenone is chemically stable, with a HOMO-LUMO energy gap of 4.89 eV, suggesting high reactivity potential. UV-Vis spectra showed that the strongest absorption at λmax = 386.29 nm (97 % contribution) was a transition from HOMO-1 to LUMO, indicating an n→π* transition. The second and third states (S2 and S3) at 359.08 nm and 278.04 nm were attributed to π→π* transitions, with 98 % and 96 %, respectively. The 13 C NMR shifts varied from 14.81 ppm for C5 to 183.18 ppm for C4, demonstrating the effect of electron-withdrawing and donating groups on shielding. The 1H NMR shifts ranged from 3.6342 to 14.557 ppm, with distinct peaks corresponding to the CH_2, CH_3, C═O, and C═C groups. ELF and LOL investigations demonstrate that electrons are highly localized in covalent areas (LOL > 0.5), as well as depletion. Docking studies showed that DMO-hexenone established hydrogen bonds with MET 4 and TRP 47 with bond lengths of 2.0 Å, 2.1 Å and 1.8 Å respectively. Both proteins exhibit anticancer activity against colon cancer by binding to DMO-hexenone −5.71 kcal/mol, which is a favourable binding energy. Future study might include experimental cytotoxicity testing to evaluate DMO-hexenone's anticancer properties as well as molecular dynamics simulations to analyse the stability of its protein interactions.

Declaration of Competing Interest

"The authors declare that they have no known competing financial interests or personal relationships that could have appeared to influence the work reported in this paper."

References

[1] V.J. RamyaDevi, G. VallalPerumal, G. Rajarajan, K. Sivakumar, V. Thanikachalam, K. Kaviyarasu, Synthesis, spectral characterization, anti-cancer activity evaluation, and molecular docking of substituted 1,2-bis(3-butyl-2,6-diphenylpiperidin-4-ylidiene) hydrazone derivatives, J.Mol.Struct. 1321 (2025) 4, https://doi.org/10.1016/j.molstruc.2024.140147.
[2] Daniel Swern, Reactions of the oxirane group, JAOCS (1970), https://doi.org/10.1007/BF02632959.
[3] Shaoke Zhang, Helfried Neumann, Matthias Beller, Synthesis of α,β-unsaturated carbonyl compounds by carbonylation reactions, Chem. Soc. Rev. 10 (2020), https://doi.org/10.1039/C9CS00615J.
[4] Laiba Arshad, Ibrahim Jantan, Syed Nasir Abbas Bukhari, Md. Areeful Haque, Immunosuppressive Effects of Natural α,β-Unsaturated Carbonyl-Based Compounds, and Their Analogs and Derivatives, on Immune Cells: A Review, 2017 Jan 30:8:22, https://doi.org/10.3389/fphar.2017.00022.
[5] Dinesh Kumar Patel, Rajesh Kumar, Damiki Laloo, Siva Hemalatha, Evaluation of phytochemical and antioxidant activities of the different fractions of hybanthus enneaspermus (linn.) f. muell. (violaceae), Asian Pac. J. Trop. Med 4 (2011), https://doi.org/10.1016/S1995-7645(11)60110-7.
[6] Dinesh K. Patel, Sairam Krishnamurthy, S. Hemalatha, Evaluation of glucose utilization capacity of bioactivity guided fractions of hybanthus enneaspermus and pedalium murex in isolated rat hemidiaphragm, J. Acute. Dis. 2 (2013), https://doi.org/10.1016/S2221-6189(13)60091-8.
[7] V.B. Narayanswamy, M. Manjunatha Setty, S. Malini, Annie shirwaikar, preliminary aphrodisiac activity of hybanthus enneaspermus in rats, Pharmacologyonline 1 (2007) 152–161, http://refhub.elsevier.com/S0022-2860(23)02054-9/sbref0004.
[8] Shakti Prasanna Sahoo, B.B. Subudhi, S. Ramchandran, M.D. Dhanraju, B. Kumaraswamy, Evaluation of anti-ulcer and anti-secretory activity of hybanthus enneaspermus, IJPRAS 1 (2012) 4, http://refhub.elsevier.com/S0022-2860(23)02054-9/sbref0008.
[9] Satheesh Kumar Dharmarajan, Kottai Muthu Arumugam, Comparative evaluation of flavone from Mucuna pruriens and coumarin from Ionidium suffruticosum for

hypolipidemic activity in rats fed with high fat diet, Lipids Health Dis. 11 (2012) 126, https://doi.org/10.1186/1476-511X-11-126.
[10] M. Arockiadoss, S. Amala, V. Yuvaraj, G. Rajarajan, K. Sivakumar, V. Thanikachalam, S. Selvanayagam, K. Kaviyarasu, Design, synthesis, structural characterization, non-linear optical and computational studies of some 3t-butyl-2r,6c-diarylpiperidin-4-on-1-ium picrates, J.Mol. Struct. 1274 (2023) 1, https://doi.org/10.1016/j.molstruc.2022.134476.
[11] S. Christopher Jeyaseelan, R. Premkumar, K. Kaviyarasu, A. Milton Franklin Benial, Spectroscopic, quantum chemical, molecular docking and in vitro anticancer activity studies on 5-methoxyindole-3-carboxaldehyde, J.Mol. Struct. 1197 (2019), https://doi.org/10.1016/j.molstruc.2019.07.042.
[12] M. Govindaraju, P. Vennila, G. Venkatesh, C. Kamal, Y. Sheena Mary, C. Yohannan Panicker, S. Kaya, Stevan Armakovic, Sanja J. Armakovic, A complete computational and spectroscopic study of 2-bromo-1, 4-dichlorobenzene - a frequently used benzene derivative, J.Mol. Struct. 1151 (2018) 245–255, https://doi.org/10.1016/j.molstruc.2017.09.049.
[13] A.D. Becke, Density-functional thermochemistry. III. the role of exact exchange, J. Chem. Phys. 98 (7) (1993) 5648–5652, https://doi.org/10.1063/1.464913.
[14] A. Suvitha, S. Periandy, S. Boomadevi, M. Govindarajan, Vibrational frequency analysis, FT-IR, FT-Raman, ab initio, HF and DFT studies, NBO, HOMO–LUMO and electronic structure calculations on pycolinaldehyde oxime, Spectrochim. Acta A Mol. Biomol. Spectrosc. 117 (2014) 216–224, https://doi.org/10.1016/j.saa.2013.07.080.
[15] S. Premkumar, A. Jawahar, T. Mathavan, M. Kumara Dhas, A. Milton Franklin Benial, Vibrational spectroscopic and DFT calculation studies of 2-amino-7-bromo5- oxo-benzopyrano [2,3-b]pyridine-3 carbonitrile, Spectrochim. Acta A Mol. Biomol. Spectrosc. (2014), https://doi.org/10.1016/j.saa.2014.11.029.
[16] Garrett M. Morris, Ruth Huey, William Lindstrom, Michel F. Sanner, Richard K. Belew, David S. Goodsell, Arthur J. Olson, Autodock4 and autodocktools4: automated docking with selective receptor flexibility, J. Comput. Chem. 30 (16) (2009), https://doi.org/10.1002/jcc.21256.
[17] Celal Tugrul Zeyrek, Selen Bilge Kocak, Huseyin Unver, Serhan Pektas, Nisan Sevin Bas, terzi, Omer Celik, Molecular structure and density functional modelling studies of 2-[(*E*)-2-(4-hydroxyphenyl)ethyliminomethyl]phenol, J.Mol. Struct. 1100 (2015) 570–581, https://doi.org/10.1016/j.molstruc.2015.07.068.
[18] Stevan Armakovi, Sanja J. Armakovi, Jovan P. Setraj, Hydrogen storage properties of sumanene, Int. J. Hydrog. 38 (2013) 12190–12198, https://doi.org/10.1016/j.ijhydene.2013.05.091.
[19] Sonia Trabelsi, Noureddine Issaoui, Silvia A. Brandan, Fehmi Bardak, Thierry Roisnel, Ahmet Atac, Houda Marouani, Synthesis and physic-chemical properties of a novel chromate compound with potential biological applications, bis(2-phenylethylammonium) chromate(VI, J.Mol. Struct. 1185 (2019) 168–182, https://doi.org/10.1016/j.molstruc.2019.02.106.
[20] Narasimhamurthy Konappa, Arakere C. Udayashankar, Soumya Krishnamurthy, Chamanalli Kyathegowda Pradeep, Srinivas Chowdappa, Sudisha Jogaiah, GC–MS analysis of phytoconstituents from Amomum nilgiricum and molecular docking interactions of bioactive serverogenin acetate with target proteins, Sci. Rep. 10 (2020) 16438, https://doi.org/10.1038/s41598-020-73442-0.
[21] Sivaraj Chandrasekaran Saraswathi Krishna, Arumugam Perumal Dhivya Dhanasekar, GCMS analysis, antioxidant and antibacterial activities of ethanol extract of anisomeles malabarica (L.) R.Br. ex. sims leaves, Asian J. Pharm. 5 (2019) 180–187, https://doi.org/10.31024/ajpp.2019.5.1.26.
[22] J.M. Dimitrić Marković, Z.S. Marković, D. Milenković, S. Jeremić, Application of comparative vibrational spectroscopic and mechanistic studies in analysis of fisetin structure, pectrochim Acta A Mol. Biomol. Spectrosc. 83 (2011) 120–129, https://doi.org/10.1016/j.saa.2011.08.001.
[23] Y.B. Ivanova, F.E. Svetoslavov, O.I. Petrov, E)-5-(3-Oxo-3-(3,4,5-trimethoxy phenyl) prop-1-en-1-yl) benzo[d]oxazol-2(3H)-one, Molbank (2024) M1866, https://doi.org/10.3390/M1866.
[24] Qilin Liu, Pu Mao, Jinwei Yuan, Yongmei Xiaoa, Liangru Yanga, Dibromido[N-(1-diethylamino-1-oxo-3-phenylpropan-2-yl)- N′-(pyridin-2-yl) imidazol-2ylidene] palladium (II) dichloromethanemono solvate, Acta Crystallogr 4 (2019), https://doi.org/10.1107/S241431461900899X.
[25] Nadeem Abad, Youness El Bakri, Jihad Sebhaoui, Youssef Ramli, El. Mokhtar Essassia, Joel T. Maguec, 1-[(Oxiran-2-yl) methyl]- 3-phenyl -1, 2-dihydro quinoxalin- 2-one, Acta Crystallogr 3 (2018), https://doi.org/10.1107/S2414314618006107.
[26] Narasimhamurthy Preveena, Amar A. Hosamani, Managutti Praveen, Gopalpur Nagendrappac, Tayur N. Guru Rowd, cis-[3-(2-Chloro-6-methylquinolin-3-yl) oxiran-2-yl] (p-tolyl) methanone, Acta Crystallogr 2 (2017), https://doi.org/10.1107/S2414314617004345.
[27] M. Khodiev, U. Holikulov, A. Jumabaev, N. ISSAOUI, L. Nikolay Lvovich, O.M. Al-Dossary, L.G. Bousiakoug, Solvent effect on the self-association of the 1,2,4-triazole: a DFT study, J.Mol. Liq. 382 (2023), https://doi.org/10.1016/j.molliq.2023.121960.
[28] R.P. Gangadharan, Molecular structure, vibrational studies and reactivity descriptors analysis of 4-[2-(tert-butylamino)-1-hydroxyethyl]-2-(hydroxymethyl) phenol trends, Sci 19 (2022), https://doi.org/10.48048/tis.2022.4912.
[29] M.A. Mumit, T.K. Pal, M.A. Alam, M.A.A.A.A. Islam, S. Paul, Sheikh, M. C. DFT studies on vibrational and electronic spectra, HOMO–LUMO, MEP, HOMA, NBO and molecular docking analysis of benzyl-3-N-(2,4,5-trimethoxyphenylmethylene) hydrazine carbodithioate, J.Mol. Struct. 1220 (2020), https://doi.org/10.1016/j.molstruc.2020.128715.
[30] Souraya Goumri-Said, Rachida Rahmani, Abdelkader Chouaih, Mohammed Benali Kanoun, Probing DCV5T-Me for organic photovoltaics: a comprehensive DFT and NEGF study, Chem. Phy. Imp. 10 (2025), https://doi.org/10.1016/j.chphi.2025.100842.
[31] M. Rocha, A. di Santo, J.M. Arias, D.M. Gil, A. Ben. Altabef, Ab-initio and DFT calculations on molecular structure, NBO, HOMO-LUMO study and a new vibrational analysis of 4-(dimethylamino) benzaldehyde, spectrochim, Acta A 136 (2015), https://doi.org/10.1016/j.saa.2014.09.077.
[32] E. Dhanalakshmi, P. Rajesh, K. Arunkumar, T. Gnanasambandan, N. ISSAOUI, K. Sudha, M. Raja, Synthesis, GCMS, spectroscopic, electronic properties, chemical reactivity, RDG, topology and biological assessment of 1-(3,6,6-trimethyl-1,6,7,7a-tetrahydrocyclopenta [c]pyran-1-yl)ethenone, Chem. Phys. 7 (2023), https://doi.org/10.1016/j.chphi.2023.100385.
[33] S. Shukla, A. Srivastava, P. Kumar, P. Tandon, R. Maurya, R.B. Singh, Vibrational spectroscopic, NBO, AIM, and multiwfn study of tectorigenin: a DFT approach, J. Mol. Struct. 1217 (2020), https://doi.org/10.1016/j.molstruc.2020.128443.
[34] J.S. Singh, M.S. Khan, S. Uddin, A DFT study of vibrational spectra of 5-chlorouracil with molecular structure, HOMO–LUMO, MEPs/ESPs and thermodynamic properties, Polym. Bull. 80 (2023), https://doi.org/10.1007/s00289-022-04181-7.
[35] M. Karabacak, Z. Cinar, M. Kurt, S. Sudha, N. Sundaraganesan, FT-IR, FT-Raman, NMR and UV–vis spectra, vibrational assignments and DFT calculations of 4-butyl benzoic acid, Spectrochim. Acta A 85 (2012), https://doi.org/10.1016/j.saa.2011.09.058.
[36] Ahmed Djafri, Fouzia Perveen, Nadia Benhalima, Nawel Khelloul, Rachida Rahmani, Ayada Djafri, Abdelkader Chouaih, Mohammed Benali Kanoun, Souraya Goumri-Said, Experimental spectral characterization, hirshfeld surface analysis, DFT/ TD-DFT calculations and docking studies of (2*Z*,5*Z*)-5-(4-nitrobenzylidene) -3-N(2-methoxyphenyl)-2-N'(2-methoxyphenylimino) thiazolidin-4-one, Heliyon 6 (2020), https://doi.org/10.1016/j.heliyon.2020.e05754.
[37] K. Gomathi, R. Rathikha, P. Rajesh, Spectroscopic (FT-IR and UV-Vis) investigation, NBO, molecular orbital and MESP analysis of 2-(4-Isobutylphenyl) propanoic acid, Chem. Bull. (2023). ⟨https://www.researchgate.net/publication/372991498⟩.
[38] Mohit Kumar, Gautam Jaiswar, Mohd Afzal 2, Mohd Muddassir, Abdullah Alarifi, Aysha Fatima, Nazia Siddiqui, Rashid Ayub, Naaser A.Y. Abduh, Waseem Sharaf Saeed and Saleem Javed, Quantum Computational, Spectroscopic (FT-IR, FT-Raman, NMR, and UV–Vis) Hirshfeld Surface and Molecular Docking-Dynamics Studies on 5-Hydroxymethyluracil.
[39] (Monomer and Trimer), Molecules, 28(5), 2116 (2023), https://doi.org/10.3390/molecules28052116.
[40] E. Dhanalakshmi, P. Rajesh, S. Suresh, M. Priyadharshini, M. Prabhaharan, Green synthesis, spectroscopic investigation, quantum chemical and molecular docking studies of 3-methylisoxazolo [4,5-b]pyridine, J.Mol. STRUCT 1298 (2024), https://doi.org/10.1016/j.molstruc.2023.136964.
[41] Jane S. Murray, Peter Politzer, Molecular electrostatic potentials and noncovalent interactions, WIREs Comput. Mol. Sci. 7 (2017), https://doi.org/10.1002/wcms.1326.
[42] Ahmed H. Radhi, Ennas A.B. Du, Fatma A. Khazaal, Zaid M. Abbas, Oday H. Aljelawi, Salam D. Hamadan, Haider A. Almashhadani, Mustafa M. Kadhim, HOMO-LUMO energies and geometrical structures effecton corrosion inhibition for organic compounds predict by DFT and PM3 methods, NeuroQuatology 18 (2020) 37–45, https://doi.org/10.14704/nq.2020.18.1.NQ20105.
[43] M. Habib Rahuman, S. Muthu, B.R. Raajaraman, M. Raja, H. Umamahesvari, Investigations on 2-(4-Cyanophenylamino) acetic acid by FT-IR,FT-raman, NMR and UV-Vis spectroscopy, DFT (NBO, HOMO-LUMO, MEP and Fukui function) and molecular docking studies, Heliyon 6 (2020), https://doi.org/10.1016/j.heliyon.2020.e04976.
[44] S. Ramalingam, M. Karabacak, S. Periandy, N. Puviarasan, D. Tanuja, Spectroscopic (infrared, raman, UV and NMR) analysis, gaussian hybrid computational investigation (MEP maps/HOMO and LUMO) on cyclohexanone oxime, Spectrochim. Acta A Mol. Biomol. Spectrosc. 96 (2020), https://doi.org/10.1016/j.saa.2012.03.090.
[45] M. Vennila, R. Rathikha, S. Muthu, A. Jeelani, Ahmad Irfan, Theoretical structural analysis (FT-IR, FT-R), solvent effect on electronic parameters NLO, FMO, NBO, MEP, UV (IEFPCM model), fukui function evaluation with pharmacological analysis on methyl nicotinate, Comput. Theor. Chem. 1217 (2022), https://doi.org/10.1016/j.comptc.2022.113890.
[46] Frank Weinhold, Discovering chemistry with natural bond orbitals, Wiley, 2012. ⟨http://refhub.elsevier.com/S0022-2860(23)01634-4/sbref0052⟩.
[47] Arulraj Ramalingam, Sivakumar Sambandam, Mouna Medimagh, Omar Al-Dossary, Noureddine Issaoui, MarekJ. Wojcik, Study of a new piperidone as an anti-Alzheimer agent: molecular docking, electronic and intermolecular interaction investigations by DFT method, J. King Saud. Univ. Sci. 33 (2021), https://doi.org/10.1016/j.jksus.2021.101632.
[48] N. Swarnalatha, S. Gunasekaran, S. Muthu, P. Rajesh, Experimental and theoretical investigations of spectroscopic properties of acitretin, Indian J. Sci. 14 (41) (2015) 43–62. ⟨https://www.researchgate.net/publication/316219558_Experimental_and_theoretical_investigations_of_spectroscopic_properties_of_acitretin⟩.
[49] Rachida Rahmani, Fouzia Perveen, Nadia Benhalima, Ahmed Djafri, Nawel Khelloul, Abdelkader Chouaih, Ayada Djafri, Mohammed Benali Kanoun, Souraya Goumri-Said, FTIR NMR and UV–visible spectral investigations, theoretical calculations, topological analysis, chemical stablity, and molecular docking study on novel bioactive compound: the 5-(5-nitro furan-2-ylmethylen), 3-n-(2-methoxy phenyl),2-n′- (2-methoxyphenyl) imino thiazolidin-4-one, POLYCYCL AROMAT COMP 43 (5) (2022) 4685–4706, https://doi.org/10.1080/10406638.2022.2094971.

[50] Pelagie Manwal A. Mekoung, Alhadji Malloum, Munusamy Govindarajan, Rose Ngono Mballa, Issofa Patouossa, Auguste Abouem A. Zintchem, Charles P. N. Nanseu, Ibrahim N. Mbouombouo, Spectroscopic properties (FT-IR NMR and UV) and DFT studies of amodiaquine, Heliyon 9 (2023), https://doi.org/10.1016/j.heliyon.2023.e22187.

[51] Seema S. Khemalapure, Vinay S. Katti, Chidanandayya S. Hiremath, Sudhir M. Hiremath, Mahantesha Basanagouda, Shivaraj B. Radder, Spectroscopic (FT-IR, FT-Raman, NMR and UV-Vis), ELF, LOL, NBO, and Fukui function investigations on (5-bromo-benzofuran-3-yl)-acetic acid hydrazide (5BBAH): experimental and theoretical approach, J.Mol. Struct. 1196 (2019), https://doi.org/10.1016/j.molstruc.2019.06.078.

[52] M. Raja, R. Raj Muhamed, S. Muthu, M. Suresh, Synthesis, spectroscopic (FT-IR, FT-raman, NMR, UV–Visible), first order hyperpolarizability, NBO and molecular docking study of (*E*)-1-(4-bromobenzylidene) semicarbazide, J.Mol. Struct. 1128 (2017), https://doi.org/10.1016/j.molstruc.2016.09.017.

[53] B. Sylaja, S. Gunasekaran, S. Srinivasan, The spectroscopic investigation, NLO, NBO NMR, HOMO–LUMO and molecular docking analysis on Clonazepam, Mater. Res. Innov. 22 (2018), https://doi.org/10.1080/14328917.2016.1278320.

[54] Thangamani Arumugam, Arulraj Ramalingam, Ahlam Roufieda Guerroudj, Sivakumar Sambandam, Nourdine Boukabcha, Abdelkader Chouaih, Conformation and vibrational spectroscopic analysis of 2,6-bis (4-fluorophenyl)-3,3-dimethylpiperidin-4-one (BFDP) by DFT method: a potent anti-parkinson's, anti-lung cancer, and anti-human infectious agent, Heliyon 9 (2023), https://doi.org/10.1016/j.heliyon.2023.e21315.

[55] S. Janani, Hemamalini Rajagopal, S. Sakthivel, S. Aayisha, M. Raja, Ahmad Irfan, Saleem Javed, S. Muthu, Molecular structure, electronic properties, ESP map (polar aprotic and polar protic solvents), and topology investigations on 1-(tert–Butoxycarbonyl)-3-piperidinecarboxylic acid- anticancer therapeutic agent, J.Mol. Struct. 1268 (2022), https://doi.org/10.1016/j.molstruc.2022.133696.

[56] R. Sukanya, D. Aruldhas, I. Hubert Joe, S. Balachandran, Spectroscopic and quantum chemical computation on molecular structure, AIM, ELF, RDG, NCI, and NLO activity of 4-VINYL benzoic acid: a DFT approach, J.Mol. Struct. 1253 (2022), https://doi.org/10.1016/j.molstruc.2021.132273.

[57] E. Dhanalakshmi, P. Rajesh, K. Arunkumar, T. Gnanasambandan, Noureddine ISSAOUI, K. Sudha, M. Raja, Synthesis, GCMS, spectroscopic, electronic properties, chemical reactivity, RDG, topology and biological assessment of 1-(3,6,6-trimethyl-1,6,7,7a-tetrahydrocyclopenta[c]pyran-1-yl)ethano, CHEM PHYS IMPACT 7 (2003), https://doi.org/10.1016/j.chphi.2023.100385.

[58] K. Vedhapriya, G. Balaji, B. Dhiyaneshwari, M. Ahmad Irfan, S. Thirunavukkarasu, Kaleeswaran, Safia Obairdur Rab, S. Muthu, Effect of green solvents, molecular structure and topological studies on 4-amino-1-β-D-ribofuranosyl-1,3,5 triazin-2 (1H)-one-anti-blood cancer agent, J. Indian Chem. Soc. 100 (2023) 100912, https://doi.org/10.1016/j.jics.2023.100912.

[59] R. Sukanya, D. Aruldhas, I. Hubert Joe, S. Balachandran, Spectroscopic and quantum chemical computation on molecular structure, AIM, ELF, RDG, NCI, and NLO activity of 4-VINYL benzoic acid: a DFT approach, J.Mol. Stuct 1253 (2022) 132273, https://doi.org/10.1016/j.molstruc.2021.132273.

[60] C. Sivakumar, V. Balachandran, B. Narayana, Vinutha V. Salian, B. Revathi, N. Shanmugapriya, K. Vanasundari, Molecular spectroscopic investigation, quantum chemical, molecular docking and biological evaluation of 2-(4-chlorophenyl)-1- [3-(4-chlorophenyl)-5-[4-(propan-2-yl) phenyl-3, 5-dihydro-1H -pyrazole-yl] ethanone, J.Mol. Stuct 1224 (2021) 129010, https://doi.org/10.1016/j.molstruc.2020.129010.

[61] Jiyu Fan, Ailing Fu, Le Zhang, Progress in molecular docking, qBio 7 (2) (2019), https://doi.org/10.1007/s40484-019-0172-y.

[62] Bel Youssouf G. Mountessou, Alain W. Ngouonpe, Alexis Sylvain W. Mbobda, Eric O. Akintemi, Hans-Georg Stammler, Simeon F. Kouam, Jean Claude Tchouankeu, Bruno N. Lenta, Norbert Sewald, Thishana Singh, Ibrahim N. Mbouombouo, Structural analysis and molecular docking study of pachypodostyflavone: a potent anti-onchocerca, J.Mol. Struct. 1291 (2023), https://doi.org/10.1016/j.molstruc.2023.136003.

[63] Robert Roskoski Jr, Properties of FDA-approved small molecule protein kinase inhibitors: a 2024 update, Pharm. Res 200 (2024), https://doi.org/10.1016/j.phrs.2024.107059.

[64] E. Dhanalakshmi a, P. Rajesh, P. Kandan, M. Kesavan, G. Jayaraman, A. Selvaraj, R. Priya, Stability of bonds, kinetic stability, energy parameters, spectral characterization, GC–MS and molecular descriptors studies on coumarine, 3-[2-(1-methyl-2-imidazolylthio)-1-oxoethyl, J.Mol. Struct. 1295 (2024), https://doi.org/10.1016/j.molstruc.2023.136544.

[65] Abir sagaama, Noureddine Issaoui, Omer A1-Dossary, Aleksandr, S. Kazachenko, MarekJ. Wojcik, Non covalent interactions and molecular docking studies on morphine compound, J. King Saud. Univ. Sci. 33 (2021), https://doi.org/10.1016/j.jksus.2021.101606.

[66] C. Prabhu, P. Rajesh, E. Dhanalakshmi, T. Gnanasambandan, M. Priyadharshini, Structure conformational, molecular docking and computational investigation of methyl linoleate, Chem. Phys. 7 (2023), https://doi.org/10.1016/j.chphi.2023.100300.

[67] Tehmina Akram, Muhammad Athar Abbasi, Ayyaz Mahmood, Edna Barboza de Lima, Fouzia Perveen, Muhammad Ashraf, Irshad Ahmad, Souraya Goumri-Said, Synthesis, molecular structure, spectroscopic properties and biological evaluation of 4-substituted-N-(1H-tetrazol-5-yl) benzenesulfonamides: combined experimental, DFT and docking study, J.Mol. Struct. 1195 (2019), https://doi.org/10.1016/j.molstruc.2019.05.065.

[68] Debnath Pal, Pinak Chakrabarti, Non-hydrogen bond interactions involving the methionine sulfur atom, J. Biomol. Struct. Dyn. 1 (2001), https://doi.org/10.1080/07391102.2001.10506725.

[69] M. Lawrence, E. Isac Paulraj, P. Rajesh, Spectroscopic characterization, electronic transitions and pharmacodynamic analysis of 1-Phenyl-1,3-butanedione: an effective agent for antipsychotic activity, Chem. Phy. Imp. 6 (2023), https://doi.org/10.1016/j.chphi.2023.100226.